Modeling alkali metal emissions in large-eddy simulation of a preheated pulverized-coal turbulent jet flame using tabulated chemistry

Kaidi Wan[1,2], Jun Xia[2,*], Luc Vervisch[3], Yingzu Liu[1], Zhihua Wang[1,*], Kefa Cen[1]

1. State Key Laboratory of Clean Energy Utilization,
Zhejiang University, Hangzhou 310027, China

2. Department of Mechanical, Aerospace and Civil Engineering & Institute of Energy Futures, Brunel University London, Uxbridge UB8 3PH, UK

3. CORIA – CNRS, Normandie Université,
INSA de Rouen, 76800 Saint-Etienne-du-Rouvray, France

* Corresponding authors: jun.xia@brunel.ac.uk (J. Xia); wangzh@zju.edu.cn (Z.H. Wang)

Word counts: 8818, excluding tables, references and captions.

Abstract

The numerical modeling of alkali metal reacting dynamics in turbulent pulverized-coal combustion is discussed using tabulated sodium chemistry in Large Eddy Simulation (LES). A lookup table is constructed from a detailed sodium chemistry mechanism including 5 sodium species, i.e., Na, NaO, NaO_2, NaOH and $Na_2O_2H_2$, and 24 elementary reactions. This sodium chemistry table contains four coordinates, i.e., the equivalence ratio, the mass fraction of the sodium element, the gas-phase temperature, and a progress variable. The table is first validated against the detailed sodium chemistry mechanism by zero-dimensional simulations. Then, LES of a turbulent pulverized-coal jet flame is performed and major coal-flame parameters compared against experiments. The chemical percolation devolatilization (CPD)

model and the partially stirred reactor (PaSR) model are employed to predict coal pyrolysis and gas-phase combustion, respectively. The response of the 5 sodium species in the pulverized-coal jet flame is subsequently examined. Finally, a systematic global sensitivity analysis of the sodium lookup table is performed and the accuracy of the proposed tabulated sodium chemistry approach has been calibrated.

Keywords: Large-eddy simulation; Tabulated chemistry; Pulverized-coal combustion; Sodium; Alkali metal

1. Introduction

Coal is used to produce approximately 40% of the worldwide electricity. In China the figure is more than 70% [1]. In the near and medium future, it can be expected that the utilization of coal will continue due to its broad availability and the overall flexibility of coal combustion systems [2]. In practice, the presence of sodium in coal leads to rapid ash deposition on heat exchangers of the boilers [3]. This high deposition rate of ash causes unscheduled shutdown of the boilers in order to clean the combustion systems to secure their efficiency [4]. Sodium species also form complex chloride and sulfur compounds, which can foul and corrode heat transfer surfaces within coal-fired boilers [5]. These sodium-induced issues severely limit the utilization of coal with a relatively high concentration of sodium, such as Zhundong coal. The newly explored 390-billion-ton Zhundong coalmine in China is able to be used for more than a century under the current consumption rate of coal [6], if the

sodium-induced fouling and corrosion issues can be overcome.

Such issue is not limited to coal. In the quest for cleaner fuels, biomass provides a renewable energy source which is foreseen as a candidate to complement fossil fuels [7]. The elemental composition of biomass, such as straw, is usually rich in potassium [8]. Since both potassium (K) and sodium (Na) belong to alkali metals, burning biomass also causes massive ash deposition, promoting corrosion in the boilers [9]. Therefore, strong motivations exist to better understand the fundamental mechanisms driving the formation and the destruction of alkali metal species during coal and biomass combustion. A better understanding of these mechanisms is important and necessary for the development of technologies ready for reducing, or capturing, these harmful species produced by coal and biomass combustion.

To understand alkali release mechanisms and reacting dynamics, online measurements using advanced laser diagnostics have been attempted recently [10, 11], together with offline measuring techniques [12], e.g. sampling measurements that can be used to analyse the bulk composition of fly ash and ash deposits. For instance, van Eyk et al. [10] developed a quantitative Planar Laser-induced Fluorescence (PLIF) technique to measure the concentration of atomic Na and its release process in the plume of a burning coal particle. It is, however, difficult to obtain the information on the release of atomic Na during the pyrolysis stage, because of the strong scattering due to soot particles. Furthermore, other sodium compounds such as NaOH and NaCl can hardly be measured simultaneously using PLIF. To overcome these limitations, Laser-induced Breakdown Spectroscopy (LIBS) was used to detect the alkali metal element (Na/K) in all relating species and measure the total released

amount. Using LIBS, the time-resolved release processes of sodium and potassium can be obtained during all coal combustion stages, including the sooting pyrolysis stage [11].

On the numerical side, the final forms of sodium species in post-combustion gases can now be modeled with well-established reaction mechanisms, as the one discussed by Glarborg and Marshall [13]. A model for sodium release during the combustion of a single Loy Yang brown coal char particle has been proposed recently [14]. However, to the best of our knowledge, the dynamic release and reaction characteristics of sodium during turbulent pulverized-coal combustion (PCC) have not been studied, despite their key role in providing important physical insights into alkali metal emissions of industrial coal-fired furnaces. Large-eddy simulation of pulverized-coal combustion (PCC-LES) has been reported in the literature as a valuable tool [15-18]. Recently, PCC-LES research has mainly focused on laboratory-scale pulverized-coal jet flames [19-23]. Tabulated flamelets have been used for modeling the flame scales unresolved by the mesh [2, 24] and studies on NO_x predictions with LES [25], which suggests that the minor chemical species, which are similar to sodium species in PCC and have much longer chemical timescales than those of the major chemical species, can be addressed within this modeling framework.

To predict sodium species in PCC-LES, two major points need to be addressed. The first one is predicting the release of sodium species from pulverized-coal particles. The amount of the sodium volatiles released from coal particles and their exact chemical composition need to be determined to provide initial conditions for the subsequent reactions of sodium species in the gas phase. In the most recent model for the release of sodium during the combustion of a

87 single Loy Yang brown coal char particle [14], the information on both the total releasable
88 amount and the exact chemical composition of the released sodium species is still out of reach.
89 In addition, the pyrolysis stage is not included in the modeling.

90 The second issue concerns the chemical kinetics of sodium species in the gas phase. As
91 noted above, a detailed reaction mechanism for sodium and potassium has been proposed by
92 Glarborg and Marshall [13]. This chemical scheme includes 105 elementary reactions, and it
93 would be computationally expensive to directly employ it in LES, instead a tabulated
94 chemistry approach is retained [26].

95 Detailed-chemistry tabulations based on canonical combustion problems, such as
96 homogeneous reactors or one-dimensional premixed or non-premixed flames, thus featuring
97 strong similarities with flamelet modeling, have received extensive attention over the past
98 fifteen years [27-31]. Based on the combination of the premixed flamelet and progress
99 variable concepts, two equivalent approaches, i.e., the flame prolongation of intrinsic
100 low-dimensional manifolds (FPI) [32] and flamelet-generated manifolds (FGM) [33] have
101 been successfully developed and employed in numerical simulations of gas [34] and
102 multiphase [35, 36] combustion [37]. In both FPI and FGM, the species distributions observed
103 through a reference flame are mapped over a progress variable, so that the knowledge of this
104 single variable is sufficient to retrieve the local flow composition. Such methodology was in
105 fact first employed in Reynolds-averaged Navier-Stokes (RANS) modeling of turbulent
106 premixed flames [38], well before chemistry tabulation was discussed *per se* in the literature.
107 In addition to modeling hydrocarbon combustion, tabulated chemistry methods have also been

applied to the prediction of minor species such as NO_x [39]. Because of the separation of time scales between the oxidation of the hydrocarbon and the production of thermal NO_x, novel approaches based on tabulated chemistry have been developed to predict NO_x [25, 34, 40]. For instance, NOMANI (Nitrogen Oxide emission model with one-dimensional MANIfold) developed by Pecquery et al. [25] uses two separate progress variables, one for hydrocarbon combustion and another for NO_x reactions.

In the present work, the second key issue of sodium predictions in PCC is addressed using detailed chemistry tabulation, namely, the introduction of the chemical kinetics of gaseous sodium species in a turbulent reacting flow. Since currently detailed information about the sodium species released from a burning coal particle is still unavailable, assumptions are formulated to provide these initial conditions. Therefore, the model that is developed will need in a close future full validation against experimental measurements.

The paper is organized as follows: details on the tabulation method for sodium chemistry are presented in Section 2, including the development and the validation of the chemical table. The LES framework is given in Section 3. The subsequent Sections 4 and 5 are devoted to the analysis of the behavior of sodium chemical species in the numerical simulation of a turbulent pulverized-coal jet flame ignited by a pilot of preheated gases. In the pulverized-coal jet flame at the laboratory scale studied in the present LES, char burnout stays limited, it could therefore be neglected [22]. A first set of LES without sodium chemistry includes char combustion. In a second set, char combustion is neglected and sodium reactions are added.

2. Tabulation of detailed sodium chemistry

2.1. Problem formulation

Because atomic sodium is predicted to be the favoured species in a flame environment [41], it is the alkali released from coal in the simulations. Moreover, because the sodium generated inside the porous structure of a coal particle will be transported outward by the volatile yielded during the pyrolysis stage, the sodium release rate is assumed to be proportional to the pyrolysis rate, or the volatile release rate (the source terms in the transport equations for volatile species mass fractions).

The detailed reaction mechanism of alkali metal species by Glarborg and Marshall [13] include 105 elementary reactions over the atomic elements Na, K, C, H, O, S and Cl. In the present study, only the subset with the atomic elements Na, C, H and O is considered, which includes 5 sodium species, i.e., Na, NaO, NaO_2, NaOH and $Na_2O_2H_2$, and 24 elementary reactions.

Apart from the reactions of sodium species, hydrocarbon volatile combustion has been modeled by a partially stirred reactor concept [42, 43]. Since the magnitude of sodium species is very small, i.e., at the ppm level, and the reactions of sodium species are slower than volatile combustion, one-way coupling is considered in the interaction between the sodium reactions and volatile combustion, i.e., the effects of hydrocarbon volatile combustion on the reactions of sodium species are considered, but the effects of sodium reactions on hydrocarbon combustion are ignored.

2.2. Table coordinates: initial conditions

The initial conditions of the chemical trajectories of sodium-related species are defined from three parameters: (i) the equivalence ratio ϕ of the mixture; (ii) the mass fraction of the sodium element Y_{sodium}; and (iii) the gas-phase temperature T. The first two allow for describing the mixing between three streams: (a) the primary pulverized-coal-particle-laden air jet, (b) the coflow and (c) the volatile stream originated from coal particles. The gas-phase temperature accounts for the effects of temperature on sodium reactions, including temperature variations due to gas-phase combustion; heat loss due to radiation; and the heat exchange between the gas and particle phases.

The range of variation, or the upper and lower bounds, of Y_{sodium} and T as table coordinates can be obtained from LES results of the pulverized-coal flame under investigation. The scatter plot in Fig. 1 shows the distribution of the mass fraction of the sodium element (Y_{sodium}) versus the equivalence ratio ϕ from an instantaneous LES result of a coflow-heated pulverized-coal jet flame studied in this work. Please note that Y_{sodium} is physically equivalent to the mass fraction of a volatile species because the release rates of volatile gas and sodium vapor are assumed to be proportional to each other (see Section 2.1). Therefore in Fig. 1, a higher Y_{sodium} also indicates that more volatile species exists at the local grid cell at each equivalence ratio. The detailed flame parameters will be given later.

The two parameters ϕ and Y_{sodium} can therefore be used to quantify the mixing among the three feeding streams in the current flame configuration. Based on the compositions of atomic C (carbon), H (hydrogen) and O (oxygen) in each of the three feeding streams, the theoretical

upper and lower bounds of Y_{sodium} can be computed and are also given in Fig. 1. The upper bound indicates a mixture of volatile and the primary air jet, and the lower bound indicates a mixture of volatile and the hot co-flow. Since the primary air jet flow carries pulverized-coal particles that generate volatile, a pure mixture between volatile and the co-flow cannot form. Since volatile is generated from a pulverized-coal particle after it is heated by the co-flow, a pure mixture between volatile and the primary air jet cannot form either. Therefore, both the theoretical upper and lower bounds are not reached by the LES results. In the present study, the two theoretical bounds have been used as the upper and lower limits of Y_{sodium} to build the chemical lookup table for sodium chemistry at each equivalence ratio.

Figure 2 shows the distribution of the gas-phase temperature (T) versus equivalence ratio. Due to the effects of the high-temperature coflow, the density of the scatter data points becomes higher in the region where the equivalence ratio is between 0 and 0.5 (Fig. 2). Also, because the gas-phase temperature is not only governed by combustion, but it is also affected by the high-temperature coflow, radiation and the heat exchange between the gas and particle phases, fluctuations of temperature exist for a fixed value of the equivalence ratio. The line plots in Fig. 2 indicate the upper and lower bounds employed in the chemical lookup table. The conditional mean and fluctuation of temperature for a given equivalence ratio lies within these bounds. Almost the whole span of the gas-phase temperature is covered by the table, except for a few data samples, which have been intentionally avoided in the lookup table. These points are very few compared to the other points and statistically they do not contribute much to the conditional mean nor to the conditional fluctuations. Moreover, the accuracy of

192 the interpolation used to retrieve data from the table decreases with the range spanned and
193 including these few points would, in the end, add more uncertainties in the modeling loop.
194 The lower bound is chosen to keep the temperature range for all the equivalence ratios less
195 than 700 K.
196
197 ***2.3. Table coordinates: progress variable***
198 After defining the three parameters characterizing the initial conditions of the trajectories
199 used to build the lookup table, the time evolution along these trajectories is remapped into a
200 progress variable space. The progress variable Y_c, representing the progress of chemical
201 reactions, is defined as a linear combination of the mass fractions of the chemical species:
202 $$Y_c(t,Z)=\sum_{i=1}^{n}\alpha_i Y_i(t,Z), \quad (1)$$
203 where Y_i is the mass fraction of the ith species, α_i is the corresponding coefficient, t is time, Z
204 denotes the initial conditions, i.e., ϕ, Y_{sodium} and T. In the present study, 5 sodium species are
205 considered. The progress variable is therefore expressed as:
206 $$Y_c(t,Z)=\alpha_1 Y_{Na}(t,Z)+\alpha_2 Y_{NaO}(t,Z)+\alpha_3 Y_{NaO2}(t,Z)+\alpha_4 Y_{NaOH}(t,Z)+\alpha_5 Y_{Na2O2H2}(t,Z). \quad (2)$$
207 For the tabulation to be effective [26], the progress variable Y_c should monotonically
208 evolve with the time t along all the chemical trajectories, so that the mass fractions of all
209 chemical species can be expressed as single-valued functions of Y_c. Then, $Y_c(t, Z)$ can be
210 uniquely inverted to $t(Y_c, Z)$, and $Y_i(t, Z) = Y_i(t(Y_c), Z)$ can then be expressed as $Y_i(Y_c, Z)$,
211 which is the evolution of chemical reactions in the progress variable space. In Niu et al. [26] it
212 was also discussed how the gradient of the species concentrations in the progress variable

space $\partial Y_i(Y_c, Z)/\partial Y_c$ should not be too large. Otherwise, a small deviation in the prediction of Y_c would lead to large errors in Y_i when reading species mass fractions in the table.

In the present case, a progress variable $Y_{c,a}$ is first defined as the total mass fraction of the sodium element present in the products of the sodium reactions. The mass of the sodium element is conserved during the sodium reactions and $Y_{c,a}$ monotonically increases along with the consumption of the reactant. Because the mass fraction of $Na_2O_2H_2$ is several orders of magnitude smaller than that of the other sodium species, $Y_{c,b}$ is added to $Y_{c,a}$ to reduce the gradient of the mass fraction of $Na_2O_2H_2$ in the progress variable space, thereby improving the accuracy of the chemistry table on the predictions of this minor sodium species.

The progress variable Y_c then reads:

$$Y_c = Y_{c,a} + Y_{c,b}, \tag{3}$$

with,

$$Y_{c,a} = (M_{NA}/M_{NAO})\, Y_{NaO} + (M_{NA}/M_{NAO2})\, Y_{NaO2} + (M_{NA}/M_{NAOH})\, Y_{NaOH} + (2M_{NA}/M_{NA2O2H2})\, Y_{Na2O2H2}, \tag{4}$$

$$Y_{c,b} = (2M_{NA}/M_{NA2O2H2})\, Y_{Na2O2H2} \times (10^4 - 1), \tag{5}$$

where M denotes the molecular weight (see Table 1). The amplification factor $(10^4 - 1)$ was determined via a trial-and-error approach to achieve the best performance of the chemistry table on tracing $Na_2O_2H_2$ and other sodium species, as shown in Section 2.5 the verification study.

2.4. Build-up of the chemical lookup table

The procedure of building up the sodium chemistry table is as follows. For each initial condition $Z(\phi, Y_{sodium}, T)$, a chemical equilibrium state of hydrocarbon combustion is computed with the open-source software CANTERA [44] together with GRI-3.0 [45], excluding the sodium reactions. Then, a zero-dimensional simulation of sodium reactions is performed using CANTERA in combination with GRI-3.0 and the detailed sodium reaction mechanism [13]. The zero-dimensional simulation is run for 2.0 seconds in total, which is much longer than the residence time of a fluid particle of the jet flow in the LES. It is also sufficiently long for the sodium reactions reaching the chemical equilibrium state except for a limited number of cases under some low-temperature conditions. The obtained chemical trajectory is then remapped into the progress variable space. Specifically, for each value of the progress variable Y_c, the corresponding concentration Y_i of the i-th sodium species and also the source term ω_{Yc} in the transport equation for the progress variable are obtained and stored into the chemistry table. ω_{Yc} is calculated based on a linear combination of the source of Y_i, using the same coefficients given in Table 1. The progress variable Y_c is normalized by the final maximum value before being stored in the table, and the normalized progress variable $C(t, Z) = Y_c(t, Z) / Y_{c,max}(2.0, Z)$ monotonically evolves from zero to unity for any single chemical trajectory of the sodium reactions. The same procedure will be looped for all the initial conditions for the obtained sodium chemistry table to include all the chemical trajectories.

The equivalence ratio ϕ in the range of 0.0 to 1.85 is discretized over 100 points on a

non-uniform grid. The grid is refined around ϕ = 1.0, where the species composition changes rapidly. For each equivalence ratio, the lower and upper limits of the mass fraction of the sodium element Y_{sodium} and gas-phase temperature T can be obtained from Figs. 1 and 2. Both of them are discretized on a uniform grid, with 30 points for Y_{sodium} and 50 for T. Finally, for the normalized progress variable C, a non-uniform grid with 100 points is used, with grid refinement at smaller C values, i.e., the initial stage of the sodium reactions, because conditions exist with strong variations in this zone. In summary, the sodium chemical table features 100 × 30 × 50 × 100 data points for $\phi \times Y_{sodium} \times T \times C$. On each of these data points the mass fractions of the 5 sodium species and the source term ω_{Yc} in the transport equation for the progress variable are stored. The size of this complete table is about 700 MB.

Figures 3-6 show the evolution of sodium reactions in the progress variable space under representative initial conditions defined by ϕ, Y_{sodium} and T. Three equivalence ratios (ϕ = 0.508, 1.0 and 1.508) are selected to illustrate fuel-lean, stoichiometric and fuel-rich flame conditions, with three typical temperatures at each equivalence ratio, to illustrate the effects of the gas-phase temperature on the sodium reactions (see Figs. 3-5).

Under fuel-lean condition (ϕ = 0.508), NaO_2 and NaOH are the main sodium products (Fig. 3). The oxidation path from Na to NaO_2 occurs through a very fast 3-body process [46]:

$$\mathrm{Na} + \mathrm{O_2}\left(+M\right) = \mathrm{NaO_2}\left(+M\right). \tag{6}$$

The NaO_2 reacts with the radicals H and OH in the products of hydrocarbon combustion, producing NaOH [46]. Figure 3 shows that the oxidation of Na towards NaO_2 is not favored at high temperature. When the temperature increases from 1005 K to 1396 K, the peak

concentration of NaO_2 decreased by almost one order of magnitude. NaOH mass fraction stays very small at the lower temperatures (1005 K in Fig. 3); but it becomes an important product at higher temperatures (1208 K and 1396 K in Fig. 3). At the end equilibrium point of the chemical trajectories, almost all the sodium is transformed into NaOH at these higher temperatures.

The source term ω_{Yc} of the progress variable that is solved with the flow is shown in Fig. 3f. Large values of ω_{Yc} at the early stage of the chemical trajectory are caused by the abovementioned fast oxidation of Na towards NaO_2. It should be noted that the source term has a relatively small but non-zero value towards the 'long tail', i.e., C = 0.1-1.0, which is illustrated in the enlarged view. As mentioned above, denser grids are used to capture the rapid variation of species trajectories in their early stage.

Figure 4 shows the evolution of sodium properties under the stoichiometric condition (ϕ = 1.0) for three temperatures (1721 K, 1878 K and 2022 K). Compared to the fuel-lean condition (Fig. 3), the most significant difference is that NaO_2 is no longer one of the major sodium products and the stiff variations at low values of the progress variable almost disappear. Indeed, because of the stoichiometric condition of the products contained in the mixture, the O_2 concentration is extremely low and the influence of the sodium oxidation reaction (6) becomes minor. At all the three temperatures, Na is gradually transformed into NaOH via reactions with hydrocarbon combustion products. As the temperature rises, the production of NaOH decreases, which indicates that the sodium reactions are again not favored at high temperature. It can also be noted that part of Na remains untransformed at the

296 end of the trajectories.

297 The evolution of the mass fractions of sodium species under fuel-rich condition (ϕ =
298 1.508) is shown in Fig. 5, also at three different temperatures (1522 K, 1629 K and 1727 K).
299 Na is gradually transformed into NaOH, and the conversion rate of Na here is much lower.
300 Besides, the values of the progress variable source term are also reduced compared to the
301 stoichiometric condition (Fig. 4), indicating an expected overall slower Na chemistry under
302 fuel-rich environment. Figure 6 shows the species response for various levels of Y_{sodium} under
303 the stoichiometric condition. The initial sodium concentration impacts on the levels of species
304 mass fractions, but does not profoundly modify the overall shape of the response versus
305 progress variable.

306

307 ***2.5. Verification of the chemistry table against detailed mechanism***

308 Before coupling the lookup-table of sodium chemistry with unsteady flow simulations,
309 verification tests are performed in which it is attempted to recover the time evolution of the
310 chemistry from solving the progress variable only (i.e. $\mathrm{d}Y_c/\mathrm{d}t = \omega_{Yc}$), species mass fractions
311 being simply read from the table. Homogeneous cases at various equivalence ratios and initial
312 conditions, in terms of sodium concentrations and temperature, are considered. Results are
313 compared against those directly obtained from the detailed chemical system [13] using
314 CANTERA and GRI-3.0. The source of the progress variable is read from the table and Y_c is
315 advanced in time with a first-order scheme. To test the multi-linear interpolations, the
316 equivalence ratios, the initial temperatures and sodium mass fractions are chosen not to be

317 exactly on the grid points of the lookup table.

318 Figures 7-9 show the comparison of the sodium chemistry predicted by the lookup table
319 against those directly obtained from the detailed mechanism. For all the 9 initial conditions
320 chosen, the predictions of the chemistry table closely follow those of the detailed chemistry
321 [13]. Minor deviations can be found in the predictions of the mass fractions of NaO and
322 $Na_2O_2H_2$ under the fuel-lean condition (Fig. 7), due to interpolation errors. However, NaO
323 and $Na_2O_2H_2$ are not major sodium species during the reactions and therefore these minor
324 errors are well acceptable. From Figs. 7-9, it can also be found that the reaction time of 2.0 s
325 is sufficient for most of the cases to reach the chemical equilibrium of the sodium reactions,
326 except for the case at the low temperature, T = 1000 K, and under the fuel-lean condition.
327 Because a duration of 2.0 seconds is much longer than the flow residence time in the jet
328 simulated thereafter, it is not necessary to include the full chemical trajectory until the
329 chemical equilibrium state for this particular case, thereby allowing us to focus the grid points
330 of the lookup table in the first stage of the chemical evolution. This verification has also been
331 performed under various other initial conditions (not shown for the sake of brevity),
332 confirming the reliability of the lookup table.

333

334 **3. Large-eddy simulation**

335 ***3.1. Gas phase modeling***

336 The filtered three-dimensional Navier-Stokes (NS) equations in the low-Mach-number
337 form for mass, momentum, species and temperature are solved for the gas phase [43, 47]. The

transport by unresolved subgrid scale (SGS) velocity fluctuations is modeled with the Germano dynamic model [48]. The balance equations for the mass fractions of N_2, O_2, H_2O, CO_2, CH_4, CO, C_2H_2, H_2, tar (9 species for coal/hydrocarbon combustion) and Y_{sodium}, Y_c (2 scalars for sodium chemistry) are solved:

$$\frac{\partial \bar{\rho} Y_n}{\partial t} + \frac{\partial \bar{\rho} u_j Y_n}{\partial x_j} = \frac{\partial}{\partial x_j}\left(\bar{\rho} \bar{D}_{iff} \frac{\partial Y_n}{\partial x_j} - q_{sgs,Y,n,j} \right) + \bar{\omega}_{Y,n} + \bar{S}_{Y,p,n}, \quad (7)$$

where $\bar{\rho}$ is the density of the gas mixture (kg/m^3), Y_n is the mass fraction of species (kg/kg), n means the nth chemical species, u_j is gas velocity (m/s), x_j is the coordinate (m), D_{iff} is the molecular mass-diffusion coefficient (m^2/s), $q_{sgs,Y,n,j}$ is the SGS term (kg/m^2 s), $\bar{\omega}_{Y,n}$ is the source term due to chemical reactions (kg/m^3 s), $\bar{S}_{Y,p,n}$ is the source term due to the discrete phase (devolatilization and surface reaction) (kg/m^3 s). It should be mentioned that for Y_{sodium}, $\bar{\omega}_{Y,n}$ is zero, because it is actually the conserved mass fraction of the sodium element originating from coal particles during sodium reactions. While for the progress variable Y_c, $\bar{S}_{Y,p,n}$ is zero and $\bar{\omega}_{Y,n}$ is obtained from the sodium-chemistry table (see Section 3.5).

Pulverized-coal particles are modeled as point sources and two-way interactions between the gas phase and particles are considered. The source terms due to coal pyrolysis, volatile combustion and char combustion in the species mass fraction equations are defined in Sections 3.3 and 3.4. In the temperature equation, the radiation, heat exchange between the gas phase and coal particles, and heat release of coal combustion are considered. In the present study, the Lewis number (Le = 1.0) and Prandtl number (Pr = 0.7) are assumed to be constant.

3.2. Particle phase modeling

The momentum equation of a coal particle in the Lagrangian framework is cast in

$$\frac{\mathrm{d}u_{p,j}}{\mathrm{d}t} = \frac{f}{\tau_p}\left(u_j - u_{p,j}\right) + W_{sgs,j}, \tag{8}$$

where $u_{p,j}$ is the velocity of the particle (m/s) and u_j is gas velocity (m/s). The dynamic response time of the particle (s) is $\tau_p = \rho_p d_p^2 / 18\bar{\mu}$, where ρ_p is the particle density (kg/m^3), and d_p is the particle diameter (m). f is the drag coefficient. Following Jones et al. [49], a stochastic Markov model is used to incorporate the effects of the unresolved SGS turbulence ($W_{sgs,j}$) into the particle acceleration.

The particle temperature is obtained by solving

$$\frac{\mathrm{d}T_p}{\mathrm{d}t} = \frac{\left(Q_{conv} + Q_{rad} + Q_{dev} + Q_{char}\right)}{m_p C_{P,p}}, \tag{9}$$

where T_p is the temperature of the particle (K), m_p the particle mass (kg). $C_{P,p}$ is the specific heat capacity (J/kg K) of the solid phase and determined by $C_{P,p} = 836.0 + 1.53\times(T_p - 273.0) - 5.4\times10^{-4}(T_p - 273.0)^2$ [47]. The heat transfer due to convection, radiation, pyrolysis (devolatilization) and char combustion is $Q_{conv} = \mathrm{Nu} C_{P,g} m_p \left(T - T_p\right) / 3\,\mathrm{Pr}\,\tau_p$, $Q_{rad} = \varepsilon_p \pi d_p^2 \sigma \left(T_R^4 - T_p^4\right)$, $Q_{dev} = -\Delta h_{dev}\,\mathrm{d}m_{vol}/\mathrm{d}t$, and $Q_{char} = -\Delta h_{char}\,\mathrm{d}m_{char}/\mathrm{d}t$, respectively, where $C_{P,g}$ is the specific heat capacity of the gas phase (J/kg K), T the gas temperature (K). Nu is the Nusselt number, calculated by the Ranz-Marshall correlations [50]. The radiation temperature (K) is estimated by $T_R = \left(G/4\sigma\right)^{1/4}$, where G is the incident radiation (W/m^2), which is determined here by the

Discrete Ordinates Method (DOM) [21, 23, 51]. σ is the Stefan-Boltzmann constant. The particle emissivity ε_p is set to 0.9 [52]. The gas absorption coefficient is determined by the weighted-sum-of-the-gray-gases model (WSGGM) [53]. The effects of the subgrid-scale gas-phase temperature and the Stefan flow on pulverized-coal-particle heating have been found to be negligible for the cases considered in the present study and therefore have not been taken into account in Q_{conv}. Finally, the rate of change of the mass of each coal particle ($\mathrm{d}m_p/\mathrm{d}t$) is equal to the sum of the coal pyrolysis rate ($\mathrm{d}m_{vol}/\mathrm{d}t$) and char combustion rate ($\mathrm{d}m_{char}/\mathrm{d}t$).

3.3. Coal pyrolysis and combustion models

The CPD model, proposed by Fletcher et al. [54], is directly incorporated into the LES framework to model the pyrolysis process of each coal particle [47]. As one of the current state-of-the-art formulation for coal pyrolysis, CPD describes the formation of volatile (including light gases and heavy tar) based on the unique chemical structure of different coals. Its performance on predicting the pyrolysis rate and volatile yield composition has been validated over a wide range of heating rates, temperatures and coal ranks [54-56]. In our previous work [52, 57], CPD was used in the pyrolysis of a single coal particle under various operating conditions. Good agreement against experimental measurements was achieved on key pyrolysis parameters, such as the time history of the particle residual mass and the temperature at the center of the particle. We also conducted further validations of the coupling of CPD with turbulent flow transport in LES and detail on its implementation may be found in

400 [43, 47]. It is briefly repeated here for completeness. The CPD model was originally
401 developed to predict the volatile yields with time. When incorporated into LES framework,
402 the variables that represent the particle pyrolysis status in the CPD model are recorded and
403 updated at every time step for each particle. When the new particle temperature is known at
404 the end of the time step, the CPD model can predict the volatile yields of the particle at the
405 new time according to the instantaneous heating rate of the particle. By subtracting the
406 volatile yields at the previous time, the volatile release of the particle in the present time step,
407 and the mass and species source terms due to the pyrolysis of the particle can be calculated.
408 The same procedure will be used for all the particles in the computational domain.

409 After the volatile matter is completely released, heterogeneous combustion of the residual
410 char occurs. The char oxidation reaction is assumed to be C (s) + 0.5 O_2 → CO, using the
411 kinetic/diffusion surface reaction model by Baum & Street [58]. Char oxidation is enabled in
412 the LES of the pulverized-coal jet flame for validation (Section 4). However, in Section 5,
413 where the sodium chemistry is investigated, the char reaction model is disabled due to very
414 limited char burnout in the turbulent jet.

415

416 ***3.4. Gas-phase combustion model***

417 Because the objective of this work is the modeling of sodium chemistry, a simple
418 description has been chosen for the turbulent burning rate controlling the heat-release in the
419 pulverized-coal turbulent flame. The LES-PaSR model [42, 43] is used for the combustion of
420 the volatiles, with a two-step reaction mechanism for the oxidation of methane [59], while

421 other species react according to a single-step chemistry [59, 60]. In this approach, the effects
422 of the unresolved SGS fluctuations of species and temperature on the non-linear burning rates
423 are accounted for by a decomposition of the turbulent flow into fine reactive/diffusive layers,
424 where most of the chemical reactions take place, and their surroundings. The volume fraction
425 of the fine structures is estimated as $\kappa = \tau_c / (\tau_c + \tau_m)$, where τ_c and τ_m are a chemical time scale
426 and a subgrid mixing time scale, respectively. The filtered reaction rate is then expressed as
427 $\bar{\omega}_{Y,n} \approx \kappa\omega(\bar{\rho}, Y_n, T)$.

428 Notice however that this description of the flame within the subgrid does not explicitly
429 account for any specific flame topologies. For example, if the gas phase equivalence ratio at
430 the LES cell center is lean and at the same time the gas at the coal surface is rich then an
431 envelope flame could exist, but it would not be resolved and would not be accounted for in
432 the convection heat transfer model in an explicit manner in the modeling.

433

434 ***3.5. Modeling sodium reactions***

435 Two variables need to be transported as two coordinates of the chemical lookup table of
436 sodium, i.e., Y_{sodium} and Y_c. The Eulerian production source of Y_{sodium} is obtained through the
437 simplified sodium release model of Section 2.1. The other two coordinates of the chemical
438 lookup table are ϕ and T. The gas-phase temperature T is directly transported in the LES
439 solver, and the equivalence ratio can be computed as

440 $$\phi = \frac{2X_{\mathrm{C}} + X_{\mathrm{H}}/2}{X_{\mathrm{O}}}, \tag{10}$$

441 where X_{C}, X_{H}, and X_{O} denote the mole fractions of atomic carbon, hydrogen and oxygen,

442 respectively. The source of the progress variable Y_c, i.e., ω_{Yc}, is read from the table to then
443 advance in time the Eulerian set of the equations. As usually done with lookup tables, Y_c is
444 normalized to define a progress variable between zero and unity. As shown above, the sodium
445 chemistry is much slower than any of the characteristic flow times. Therefore, mesh nodes
446 values are directly used without accounting for unresolved SGS fluctuations.

447 The chemical lookup table, which is based on trajectories obtained for a fixed value of
448 the temperature, cannot account for the variations of the sodium compositions at a chemical
449 equilibrium (the progress variable equals unity) due to the evolution of the local temperature.
450 To track these additional variations of the progress of sodium reactions, a term has been added
451 to ω_{Yc} to consider the relaxation towards the new equilibrium conditions. Following Galpin et
452 al. [61], the additional source term can be written as:

453 $$\omega_{Y_c}^{\mathrm{RTE}} = \frac{Y_c^{\mathrm{Eq}}\left(\bar{\phi}, Y_{sodium}, T\right) - Y_c}{\gamma \delta t} \tag{11}$$

454 where δt is the time step used in the LES solver, γ is a relaxation coefficient. Then the source
455 term of the progress variable reads:

456 $$\bar{\omega}_{Y_c} = \omega_{Y_c}^{\mathrm{TAB}}\left(\bar{\phi}, Y_{sodium}, T\right) + \beta \omega_{Y_c}^{\mathrm{RTE}} \tag{12}$$

457 with $\beta = 0$ as long as the sodium reactions do not reach chemical equilibrium, i.e., $Y_c < Y_c^{\mathrm{Eq}}$,
458 otherwise $\beta = 1$. $\omega_{Y_c}^{\mathrm{TAB}}$ is the source term obtained from the lookup table. The value of γ is
459 set to be 1.0 in the present study.

460

3.6. Numerical schemes

The time advancement uses a second-order Crank-Nicolson scheme. All terms in the momentum equations, and the scalar diffusion terms in the species and temperature equations, are discretized with a second-order central-difference scheme. To secure scalar boundedness, a third-order weighted essentially non-oscillatory (WENO) scheme [62] is used for the advection terms in the species and temperature equations [63].

4. LES of a pulverized-coal jet flame: validation

The pulverized-coal turbulent jet flame experimentally and numerically studied in [64] and [19, 20] is simulated. The laboratory-scale coflow-heated pulverized-coal jet flame was measured at the Hitachi Power & Industrial Systems R& D Laboratory [64]. A mixture of pulverized-coal particles and air are injected through a central nozzle, the inner diameter of which is 7 mm. The Reynolds number of the primary air jet is about 4500. To stabilize the pulverized-coal jet flame, hot coflow gas produced by catalytic combustion of propane is used to ignite coal particles. A high-speed camera was employed to capture the ignition phenomena of the pulverized-coal jet and the lift-off height was then determined from the images. Gas temperature was measured by a Pt/Pt-Rh thermocouple with a diameter of 100 μm and corrected for heat loss of radiation. Coal burnout was measured by collecting and analyzing burning particles using a stainless-steel water cooling sampling probe with an inner diameter of 10 mm.

4.1. Computational setup

The computational domain spans 500 mm in length and 300 mm in width. The mesh contains 1.52 million cells, whose characteristic size varies between 0.3 mm (e.g., at the edge of the nozzle and in the main reaction zones) and 5.2 mm (e.g., at the downstream exit of the domain). After reaching a resolution of 300 μm at the edge of the nozzle, the statistical flow properties collected from LES have been found weakly sensitive to grid resolution.

The operating conditions are summarized in Table 2. The primary inlet is located at the center of the $x = 0$ face (x is the streamwise direction), with a nozzle diameter (D) of 7 mm. Cold air (300 K) and coal particles are injected through this nozzle. The coal particles are ignited by the coflowing preheated gas (1510 K). To provide the relevant inflow boundary conditions for the LES, a separate, pre-processed pipe-flow LES with periodic streamwise boundary conditions has been carried out to generate an inflow database [65]. Convective boundary conditions are applied at the streamwise exit of the domain, while zero-gradient boundary conditions are applied at the side of the domain. A particle size distribution given by Yamamoto et al. [19] is prescribed at the inlet. The location of a given particle injected at the nozzle is determined according to a random uniform distribution over the primary inlet face, while its velocity equals the local gas velocity. The coal analysis data [19] is listed in Table 3. The initial density of coal particles is 1400 kg/m^3 [20]. Three inlet stoichiometric ratios (SRs) are considered (0.14, 0.22, 0.36) by varying the coal mass flow rate, where the SR is defined as: SR = (the inlet oxygen mass) / (oxygen mass that is required for completely burning the coal at the inlet).

503

504 ***4.2. Results and discussion***

505 *4.2.1. Instantaneous gas temperature*

506 The instantaneous gas temperature fields of the pulverized-coal jet flame at three different
507 SRs are shown in Fig. 10. Similar to the findings in [19], three combustion regions can be
508 observed in the ignition process. The first one is governed by heat-transfer (turbulent mixing
509 and radiation) between the flow and the particles (pre-heating region). There only some
510 isolated flame structures (IFSs) are observed. Some particles with relatively small diameters
511 are ignited at first on the jet periphery, i.e. in the mixing layer with the hot-coflow, but the
512 heat release is not strong enough to ignite adjacent coal particles, which results in the reported
513 isolated burning flow areas. The second is a growing flame (GF) region, where more and
514 more particles ignite, followed by a rapid spreading of the flame. The final one is a
515 continuous flame (CF) region, where the pulverized-coal jet flame achieves a stable
516 combustion state. As the inlet air/fuel stoichiometric ratio increases, the ignition position of
517 the pulverized-coal jet flame moves further downstream, and the flame tends to be weaker.

518

519 *4.2.2. Quantitative comparisons on the flame characteristics*

520 Following Yamamoto et al. [19], the pulverized-coal jet is considered to be ignited when
521 the gas temperature reaches 1560 K, which is 50 K higher than the preheated co-flow gas
522 temperature. The lift-off height is then defined as the distance from the primary nozzle exit to
523 the location where the growing flame region and the iso-surface of the ignition temperature (*T*

524 = 1560 K) appear. As shown in Fig. 11, the lift-off heights predicted by the present CPD-LES
525 at three different SRs are in good agreement with the experimental data [64] and the LES
526 results of Yamamoto et al. (LES-Yamamoto) [19].

527 Figure 12 compares the mean gas temperature along the jet centerline against the
528 experimental measurements and previous LES by Yamamoto et al. for SR = 0.14. Above the
529 streamwise location x = 100 mm, the collected statistics agree well with the experimental data
530 and previous LES. For x < 100 mm, which is the preheating region, the temperature increase
531 on the centerline is slower in the actual CPD-LES than in the previously reported LES, with
532 an underestimation of the temperature compared to the measurements at x = 100 mm. The
533 deviation may be due to the inflow boundary conditions of the LES.

534 Figure 13 shows the comparison of the coal burnout along the centerline at SR = 0.22.
535 Both the CPD-LES and LES by Yamamoto et al. achieve good agreement with the
536 experimental data at x = 50, 150 and 400 mm. However, the two LES methods give different
537 predictions in the region of 150 < x < 400 mm. Compared with the experimental data, the
538 present CPD-LES slightly over-predicts the coal burnout at x = 300 mm, for which the LES
539 by Yamamoto et al. under-predicts. It is found that at x = 400 mm the coal burnout by char
540 combustion is only 4.2% (daf basis), and this value is 1.9% in the LES results of Yamamoto
541 et al. (not shown in the figure). Since the influence of char combustion is weak compared to
542 pyrolysis in this pulverized-coal jet flame [19], the difference between the two LES results is
543 mainly due to the prediction of pyrolysis. The CPD model used in the present simulations
544 predicts faster pyrolysis mechanisms compared to the modified SFOM pyrolysis model [19,

66] used in the LES by Yamamoto et al. [19]. Despite these departures, which are unavoidable considering the complexity of the physical phenomena that need to be addressed in coal combustion, overall these simulations capture the global flame structure, which allows for proceeding with the introduction of the modeling of sodium chemistry in the turbulent flame.

5. Sodium reacting dynamics in a pulverized-coal jet flame

5.1. Computational setup

The computational setup is similar to that of Section 4.1 except for some minor adjustments. Properties of Loy Yang brown coal are used, for which sodium data are available [67]. Its coal analysis data are listed in Table 4. The mass fraction of the sodium element in the coal is 0.067%. The percentage of sodium that is releasable during the coal pyrolysis stage is set to 19.1%, according to [67]. Then the proportional factor of sodium release to volatile release can be determined as 0.067% × 19.1% × m_p / m_{vol}, where m_p is the mass of a pulverized-coal particle and m_{vol} is the mass of volatile yields. The char reaction model is turned off because it was found to weakly contribute in this turbulent flame. The inlet stoichiometric ratio SR = 0.22 is considered.

5.2. Results and discussion

A snapshot of the turbulent pulverized-coal jet flame is shown in Fig. 14. Only 0.1% of the total number of particles is plotted. Each particle is colored by its temperature and its size

566 in this plot is proportional to its diameter. The gas-phase temperature field is also shown. As
567 in the simulations reported above, after their injection with the cold primary air jet, the coal
568 particles are gradually heated up by the high-temperature coflow. Then, pyrolysis takes place
569 and the discrete solid phase releases volatiles. These gaseous volatile fuels are subsequently
570 ignited to burn around the pulverized-coal particles, which will further enhance the pyrolysis
571 reaction and helps achieve stable combustion of the pulverized-coal jet.

572 Sodium is released along with volatile species during the coal pyrolysis process. The
573 mass fraction of NaOH, one of the major sodium species, is shown on the left side of Fig. 14,
574 with the isoline of ϕ = 1 superimposed. The equivalence ratio ϕ is calculated based on the
575 molar fractions of atomic carbon, hydrogen and oxygen (see Eq.(10)). It is therefore
576 conserved during gas-phase combustion, but not conserved during turbulent mixing. Since the
577 equivalence ratio is zero for the primary air jet and small (= 0.52) for the coflow, large values
578 of ϕ are mainly due to the volatile stream originating from coal particles (Fig. 15). The isoline
579 of ϕ = 1 denotes the stoichiometric condition for reactions between the volatile fuels and the
580 oxidizer, which also indicates the region of the highest temperature (Figs. 14 and 2). From Fig.
581 14, it can be seen that NaOH is formed in both fuel-lean (outside the isoline) and fuel-rich
582 (inside the isoline) regions. The highest NaOH concentration is observed in the regions close
583 to the iso-surface defined by ϕ = 1, which is in accordance with the results shown in Figs. 7-9.

584 Figure 16 shows the instantaneous fields of the mass fractions of the other 4 sodium
585 species, i.e., Na, NaO, NaO_2 and $Na_2O_2H_2$, still together with the isoline of ϕ = 1. It is seen
586 that Na, the atomic sodium, features a higher concentration in fuel-rich regions (Fig. 16a).

587 This is explained by the fact that Na is the assumed outgassing species released along with the
588 volatiles from coal particles, accordingly Na is favored in a fuel-rich environment, as also
589 reported above in Figs. 7-9. NaO is found to be produced under the stoichiometric condition
590 ($\phi = 1$), but the magnitude of its mass fraction is two orders of magnitude lower than those of
591 Na and NaOH (Fig. 16b). Both NaO_2 (Fig. 16c) and $Na_2O_2H_2$ (Fig. 16d) are then rather
592 generated under fuel-lean conditions. However, the concentration of NaO_2 reaches a
593 considerably higher value near the ignition region of the pulverized-coal jet flame – a flow
594 zone where sodium vapor is already generated from coal particles, but the temperature is still
595 low. Finally, the concentration of $Na_2O_2H_2$ is found to be very low in the whole domain.

596 The mean and RMS mass fractions of the 5 sodium species along the jet centerline are
597 shown in Fig. 17, with the fuel-lean and fuel-rich regions also illustrated. For the mean mass
598 fractions, it can be found that Na features a single-peak distribution along the centerline and
599 has the highest concentration among the 5 sodium species in the fuel-rich region; while the
600 profile of Y_{NaOH} is a double-peak distribution with the peak concentrations achieved in the
601 stoichiometric regions. The concentration of NaO_2 can be considerably high in the fuel-lean
602 regions but very minor in the fuel-rich region. Finally, the concentrations of NaO and
603 $Na_2O_2H_2$ stay very low all along the centerline, similar to their instantaneous mass fractions
604 illustrated in Fig. 16. For the RMS mass fractions, the fluctuations of the 5 sodium species
605 can achieve the same order of magnitude as the corresponding mean values, which indicates
606 the distribution of the sodium species is considerably affected by the turbulence. The highest
607 fluctuation of Na is found near the upstream stoichiometric region, where the pulverized-coal

608 jet is ignited. The turbulence of the jet flow leads to the instability of the ignition process and
609 then results in a high fluctuation of sodium release.
610
611 ***5.3. Sensitivity analysis of the tabulated sodium chemistry***
612 To investigate the uncertainties of the sodium species results predicted by the tabulated
613 sodium chemistry approach, a systematic global sensitivity analysis [68] has been performed.
614 Considering the computational cost of performing such a global sensitivity analysis study
615 directly on LES would be very high, here a systematic quantification of the uncertainties
616 generated by the sodium lookup table and the global sensitivity of sodium species results to
617 the variation of the four table input parameters (ϕ, Y_{sodium}, T and C) have been assessed.
618 Three representative conditions (see Table 5), which illustrate fuel-lean, stoichiometric
619 and fuel-rich flame conditions, are selected to perform the uncertainty quantification and
620 global sensitivity analysis. The mean values of Y_{sodium} and T are typical values at each
621 condition, while the mean values of C are set as 0.5 to represent the midpoint of the sodium
622 reactions. The uncertainty range of ϕ, Y_{sodium}, T and C is determined considering the available
623 values stored in the chemistry table, the empirical magnitude of the uncertainty and also the
624 discrepancy between the LES and experimental measurements in Section 4 the validation
625 study. All the input uncertain parameters are described by a semicircle Beta distribution
626 ($Beta(3/2, 3/2)$) to avoid unrealistic values that could easily appear with a Normal distribution
627 [69]. 10,000 random sampling values are generated from the Beta distribution for each
628 uncertain parameter and used as the chemistry table inputs. The response sodium species

629 results from the chemistry table are then collected and analyzed. Figure 18 illustrates the
630 mean mass fractions of the 5 sodium species along with the standard deviations under the
631 fuel-lean, stoichiometric and fuel-rich conditions. For the two major sodium species NaOH
632 and Na predicted in the pulverized-coal jet flame, the uncertainty of their mass fractions is
633 found to be small. Considering the other sodium species, the uncertainty of Y_{NaO2} is also small
634 under the fuel-lean condition. NaO_2 is known from Fig. 17 to mainly form in fuel-lean regions
635 in the flame; while the uncertainties of Y_{NaO} and $Y_{Na2O2H2}$ can be large.

636 An optimized Monte Carlo method proposed by Sobol' et al. [70] has been employed to
637 compute the first-order main-effect sensitivity indices [71], which quantify the contribution of
638 each uncertain parameter (ϕ, Y_{sodium}, T and C) to the uncertainty of the 5 sodium species.
639 Figures 19-21 shows the obtained main-effect sensitivity indices under the fuel-lean,
640 stoichiometric and fuel-rich conditions. It can be observed that the predicted mass fractions of
641 NaOH and Na are strongly sensitive to Y_{sodium} under the fuel-lean and fuel-rich conditions,
642 respectively. Since Y_{sodium} is determined from the sodium release model during the LES, it
643 means the accuracy of the predictions of the two major sodium species NaOH and Na can
644 benefit from a more accurate sodium release model. A similar phenomenon is observed for
645 NaO_2 in the fuel-lean condition. For the minor sodium species NaO and $Na_2O_2H_2$, the
646 prediction of the tabulated sodium chemistry approach is found to be highly sensitive to the
647 temperature in the fuel-lean and fuel-rich conditions. Finally, all the 5 sodium species are
648 found to have a significant sensitivity to ϕ under the stoichiometric condition. This result can
649 be anticipated since a small uncertainty of ϕ can result in a large variation of the gas

650 compositions near the stoichiometric condition, which in turn leads to a significant impact on
651 the sodium reactions.
652
653 **6. Conclusions**
654 A tabulated chemistry method for predicting sodium species in LES of turbulent
655 pulverized-coal combustion has been discussed. One-way coupling is used for the interaction
656 between the sodium reactions and volatile combustion, i.e., the former having no influence on
657 the latter, which is expected because of the large difference in both their respective
658 characteristic time scales and their relative contribution to the total mass. In a first
659 approximation, the sodium release rate from a pulverized-coal particle is also assumed to be
660 proportional to the pyrolysis rate. The chemical lookup table is built from a series of
661 zero-dimensional simulations, which are representative of the time evolution of sodium
662 species mass fractions in a detailed chemistry mechanism [13], which includes 5 sodium
663 species, i.e., Na, NaO, NaO_2, NaOH and $Na_2O_2H_2$, reacting over 24 elementary reactions.
664 Three parameters, i.e., the equivalence ratio, the mass fraction of the sodium element and the
665 gas-phase temperature, define the initial conditions of these chemical trajectories. The three
666 parameters, along with the progress variable that represents the progress of sodium reactions,
667 are then the four coordinates of the sodium chemical lookup table. A preliminary verification
668 study of the tabulation strategy has been reported, in which the species mass fractions
669 retrieved from solving the time evolution of the single progress variable are compared against
670 the fully detailed chemistry solutions.

671 The sodium chemistry table is then coupled to LES in the configuration of a laboratory
672 pulverized-coal turbulent jet flame for which experimental results of major coal-flame
673 parameters exist. Statistics are collected and results compared against measurements and
674 previous simulations of the literature. Good agreements between the experimental
675 measurements and the LES results have been achieved on gas temperature and lift-off height,
676 while the LES tends to slightly over-predict the coal burnout. In a second part, the combustion
677 of the Loy Yang brown coal is simulated, for which sodium data are available. The results
678 show that Na and NaOH are the two major sodium species in the pulverized-coal turbulent jet
679 flame. Na, the atomic sodium, has a high concentration in fuel-rich regions; while the highest
680 NaOH concentration is found in regions close to the stoichiometric condition. The
681 fluctuations of the 5 sodium species can achieve the same order of magnitude as the
682 corresponding mean values at the jet centerline, indicating the distribution of the sodium
683 species is considerably affected by the turbulence of the jet flow. The accuracy of the
684 proposed tabulated sodium chemistry approach has been calibrated via a systematic global
685 sensitivity analysis of the sodium lookup table. The uncertainties of the two major sodium
686 species Na and NaOH are found to be small. The predicted mass fractions of Na and NaOH
687 have a strong sensitivity to the sodium release, which means the accuracy of the predictions of
688 the two major sodium species can benefit from a more accurate sodium release model.
689 In the perspective of this modeling work, developing sodium species measurements in
690 pulverized-coal laboratory jet-flames appears as a mandatory step, in order to perform further
691 validation against experimental data and gain more confidence in the proposed modeling.

692 Finally, it should be pointed out that the proposed formalism can be readily extended to the
693 modeling of the emission of potassium in turbulent multiphase biomass combustion.
694
695 **Acknowledgements**
696 This work was performed by the first author KDW when he was a Research Assistant at
697 Brunel University London under the support of the Royal Society, the Engineering and
698 Physical Sciences Research Council (EPSRC) of the UK and the China Scholarship Council.
699 The research was also supported by National Natural Science Foundation of China (51390491,
700 51422605). Special thanks are due to Prof. Peter Glarborg of Technical University of
701 Denmark, who provided us the detailed chemical mechanism of alkali metal species. This
702 work used the ARCHER UK National Supercomputing Service (http://www.archer.ac.uk).
703
704 **References**
705 [1] R. Khatami, and Y.A. Levendis, *An overview of coal rank influence on ignition and*
706 *combustion phenomena at the particle level*, Combust. Flame 164 (2016), pp. 22-34.
707 [2] R. Knappstein, G. Kuenne, A. Ketelheun, J. Köser, L. Becker, S. Heuer, M. Schiemann,
708 V. Scherer, A. Dreizler, A. Sadiki, and J. Janicka, *Devolatilization and volatiles reaction*
709 *of individual coal particles in the context of FGM tabulated chemistry*, Combust. Flame
710 169 (2016), pp. 72-84.
711 [3] S. Jiang, L. Shen, X. Niu, H. Ge, and H. Gu, *Chemical Looping Co-combustion of*
712 *Sewage Sludge and Zhundong Coal with Natural Hematite as the Oxygen Carrier*,
713 Energy Fuels 30 (2016), pp. 1720-1729.
714 [4] X. Wu, X. Zhang, K. Yan, N. Chen, J. Zhang, X. Xu, B. Dai, J. Zhang, and L. Zhang,
715 *Ash deposition and slagging behavior of Chinese Xinjiang high-alkali coal in 3 MWth*
716 *pilot-scale combustion test*, Fuel 181 (2016), pp. 1191-1202.
717 [5] Y. He, K.Z. Qiu, R. Whiddon, Z.H. Wang, Y.Q. Zhu, Y.Z. Liu, Z.S. Li, and K.F. Cen,
718 *Release characteristic of different classes of sodium during combustion of Zhun-Dong*
719 *coal investigated by laser-induced breakdown spectroscopy*, Sci. Bull. 60 (2015), pp.
720 1927-1934.
721 [6] G. Song, X. Qi, W. Song, and Q. Lu, *Slagging Characteristics of Zhundong Coal during*

Circulating Fluidized Bed Gasification, Energy Fuels 30 (2016), pp. 3967-3974.

[7] M. Bläsing, and M. Müller, *Investigation of the effect of alkali metal sorbents on the release and capture of trace elements during combustion of straw*, Combust. Flame 160 (2013), pp. 3015-3020.

[8] L. Hindiyarti, F. Frandsen, H. Livbjerg, P. Glarborg, and P. Marshall, *An exploratory study of alkali sulfate aerosol formation during biomass combustion*, Fuel 87 (2008), pp. 1591-1600.

[9] B. Li, Z. Sun, Z. Li, M. Aldén, J.G. Jakobsen, S. Hansen, and P. Glarborg, *Post-flame gas-phase sulfation of potassium chloride*, Combust. Flame 160 (2013), pp. 959-969.

[10] P.J. van Eyk, P.J. Ashman, Z.T. Alwahabi, and G.J. Nathan, *Simultaneous measurements of the release of atomic sodium, particle diameter and particle temperature for a single burning coal particle*, Proc. Combust. Inst. 32 (2009), pp. 2099-2106.

[11] Y. He, J.J. Zhu, B. Li, Z.H. Wang, Z.S. Li, M. Aldén, and K.F. Cen, *In-situ measurement of sodium and potassium release during oxy-fuel combustion of lignite using laser-induced breakdown spectroscopy: effects of O2 and CO2 concentration*, Energy Fuels 27 (2013), pp. 1123-1130.

[12] R.J. Quann, M. Neville, M. Janghorbani, C.A. Mims, and A.F. Sarofim, *Mineral matter and trace-element vaporization in a laboratory-pulverized coal combustion system*, Environ. Sci. Technol. 16 (1982), pp. 776-781.

[13] P. Glarborg, and P. Marshall, *Mechanism and modeling of the formation of gaseous alkali sulfates*, Combust. Flame 141 (2005), pp. 22-39.

[14] P.J. van Eyk, P.J. Ashman, and G.J. Nathan, *Mechanism and kinetics of sodium release from brown coal char particles during combustion*, Combust. Flame 158 (2011), pp. 2512-2523.

[15] R. Kurose, H. Watanabe, and H. Makino, *Numerical simulations of pulverized coal combustion*, KONA Powder Part. J. 27 (2009), pp. 144-156.

[16] P. Edge, S.R. Gubba, L. Ma, R. Porter, M. Pourkashanian, and A. Williams, *LES modelling of air and oxy-fuel pulverised coal combustion—impact on flame properties*, Proc. Combust. Inst. 33 (2011), pp. 2709-2716.

[17] M. Gharebaghi, R.M.A. Irons, L. Ma, M. Pourkashanian, and A. Pranzitelli, *Large eddy simulation of oxy-coal combustion in an industrial combustion test facility*, Int. J. Greenh. Gas Control 5 (2011), pp. S100-S110.

[18] L. Chen, and A.F. Ghoniem, *Simulation of oxy-coal combustion in a 100 kWth test facility using RANS and LES: a validation study*, Energy Fuels 26 (2012), pp. 4783-4798.

[19] K. Yamamoto, T. Murota, T. Okazaki, and M. Taniguchi, *Large eddy simulation of a pulverized coal jet flame ignited by a preheated gas flow*, Proc. Combust. Inst. 33 (2011), pp. 1771-1778.

[20] J. Pedel, J.N. Thornock, and P.J. Smith, *Large eddy simulation of pulverized coal jet flame ignition using the direct quadrature method of moments*, Energy Fuels 26 (2012), pp. 6686-6694.

[21] B.M. Franchetti, F. Cavallo Marincola, S. Navarro-Martinez, and A.M. Kempf, *Large eddy simulation of a pulverised coal jet flame*, Proc. Combust. Inst. 34 (2013), pp.

765 2419-2426.
766 [22] O.T. Stein, G. Olenik, A. Kronenburg, F.C. Marincola, B.M. Franchetti, A.M. Kempf, M.
767 Ghiani, M. Vascellari, and C. Hasse, *Towards comprehensive coal combustion modelling*
768 *for LES*, Flow Turbul. Combust. 90 (2013), pp. 859-884.
769 [23] M. Rabaçal, B.M. Franchetti, F.C. Marincola, F. Proch, M. Costa, C. Hasse, and A.M.
770 Kempf, *Large Eddy Simulation of coal combustion in a large-scale laboratory furnace*,
771 Proc. Combust. Inst. 35 (2015), pp. 3609-3617.
772 [24] J. Watanabe, and K. Yamamoto, *Flamelet model for pulverized coal combustion*, Proc.
773 Combust. Inst. 35 (2015), pp. 2315-2322.
774 [25] F. Pecquery, V. Moureau, G. Lartigue, L. Vervisch, and A. Roux, *Modelling nitrogen*
775 *oxide emissions in turbulent flames with air dilution: Application to LES of a*
776 *non-premixed jet-flame*, Combust. Flame 161 (2014), pp. 496-509.
777 [26] Y.S. Niu, L. Vervisch, and P.D. Tao, *An optimization-based approach to detailed*
778 *chemistry tabulation: Automated progress variable definition*, Combust. Flame 160
779 (2013), pp. 776-785.
780 [27] J.A. van Oijen, F.A. Lammers, and L.P.H. de Goey, *Modeling of complex premixed*
781 *burner systems by using flamelet-generated manifolds*, Combust. Flame 127 (2001), pp.
782 2124-2134.
783 [28] E. Knudsen, and H. Pitsch, *A general flamelet transformation useful for distinguishing*
784 *between premixed and non-premixed modes of combustion*, Combust. Flame 156 (2009),
785 pp. 678-696.
786 [29] K. Wang, G. Ribert, P. Domingo, and L. Vervisch, *Self-similar behavior and chemistry*
787 *tabulation of burnt-gas diluted premixed flamelets including heat-loss*, Combust. Theory
788 Model. 14 (2010), pp. 541-570.
789 [30] K.K.J. Ranga Dinesh, X. Jiang, and J.A. van Oijen, *Numerical simulation of hydrogen*
790 *impinging jet flame using flamelet generated manifold reduction*, Int. J. Hydrogen
791 Energy 37 (2012), pp. 4502-4515.
792 [31] D. Moëll, D. Lörstad, and X.S. Bai, *Numerical Investigation of Methane/Hydrogen/Air*
793 *Partially Premixed Flames in the SGT-800 Burner Fitted to a Combustion Rig*, Flow
794 Turbul. Combust. 96 (2016), pp. 987-1003.
795 [32] O. Gicquel, N. Darabiha, and D. Thévenin, *Liminar premixed hydrogen/air counterflow*
796 *flame simulations using flame prolongation of ILDM with differential diffusion*, Proc.
797 Combust. Inst. 28 (2000), pp. 1901-1908.
798 [33] J.A. van Oijen, and L.P.H. de Goey, *Modelling of Premixed Laminar Flames using*
799 *Flamelet-Generated Manifolds*, Combust. Sci. Technol. 161 (2000), pp. 113-137.
800 [34] A.W. Vreman, B.A. Albrecht, J.A. van Oijen, L.P.H. de Goey, and R.J.M. Bastiaans,
801 *Premixed and nonpremixed generated manifolds in large-eddy simulation of Sandia*
802 *flame D and F*, Combust. Flame 153 (2008), pp. 394-416.
803 [35] M. Chrigui, J. Gounder, A. Sadiki, A.R. Masri, and J. Janicka, *Partially premixed*
804 *reacting acetone spray using LES and FGM tabulated chemistry*, Combust. Flame 159
805 (2012), pp. 2718-2741.
806 [36] E. Knudsen, Shashank, and H. Pitsch, *Modeling partially premixed combustion behavior*
807 *in multiphase LES*, Combust. Flame 162 (2015), pp. 159-180.

[37] P.D. Nguyen, L. Vervisch, V. Subramanian, and P. Domingo, *Multidimensional flamelet-generated manifolds for partially premixed combustion*, Combust. Flame 157 (2010), pp. 43-61.
[38] D. Bradley, L.K. Kwa, A.K.C. Lau, M. Missaghi, and S.B. Chin, *Laminar flamelet modeling of recirculating premixed methane and propane-air combustion*, Combust. Flame 71 (1988), pp. 109-122.
[39] D. Bradley, P.H. Gaskell, X.J. Gu, M. Lawes, and M.J. Scott, *Premixed turbulent flame instability and NO formation in a lean-burn swirl burner*, Combust. Flame 115 (1998), pp. 515-538.
[40] G. Godel, P. Domingo, and L. Vervisch, *Tabulation of NOx chemistry for Large-Eddy Simulation of non-premixed turbulent flames*, Proc. Combust. Inst. 32 (2009), pp. 1555-1561.
[41] S. Srinivasachar, J.J. Helble, D.O. Ham, and G. Domazetis, *Ash Deposition A kinetic description of vapor phase alkali transformations in combustion systems*, Prog. Energy Combust. Sci. 16 (1990), pp. 303-309.
[42] M. Berglund, E. Fedina, C. Fureby, J. Tegnér, and V. Sabel'nikov, *Finite Rate Chemistry Large-Eddy Simulation of Self-Ignition in Supersonic Combustion Ramjet*, AIAA J. 48 (2010), pp. 540-550.
[43] K.D. Wan, J. Xia, Z.H. Wang, M. Pourkashanian, and K.F. Cen, *Large-eddy Simulation of Pilot-assisted Pulverized-coal Combustion in a Weakly Turbulent Jet*, Flow Turbul. Combust. 99 (2017), pp. 531-550.
[44] D.G. Goodwin, H.K. Moffat, and R.L. Speth, *Cantera: An object-oriented software toolkit for chemical kinetics, thermodynamics, and transport processes*, Version 2.2.1, 2016. Available at http://www.cantera.org.
[45] G.P. Smith, D.M. Golden, M. Frenklach, N.W. Moriarty, B. Eiteneer, M. Goldenberg, C.T. Bowman, R.K. Hanson, S. Song, W.C. Gardiner Jr., V.V. Lissianski, and Z. Qin, *GRI-Mech 3.0*. Available at http://www.me.berkeley.edu/gri_mech/.
[46] K. Schofield, and M. Steinberg, *Sodium/sulfur chemical behavior in fuel-rich and -lean flames*, J. Phys. Chem. 96 (1992), pp. 715-726.
[47] K.D. Wan, J. Xia, Z.H. Wang, L.C. Wrobel, and K.F. Cen, *Online-CPD-coupled large-eddy simulation of pulverized-coal pyrolysis in a hot turbulent nitrogen jet*, Combust. Sci. Technol. 189 (2017), pp. 103-131.
[48] M. Germano, U. Piomelli, P. Moin, and W.H. Cabot, *A dynamic subgrid‐scale eddy viscosity model*, Phys. Fluids A 3 (1991), pp. 1760-1765.
[49] W.P. Jones, S. Lyra, and S. Navarro-Martinez, *Large Eddy Simulation of a swirl stabilized spray flame*, Proc. Combust. Inst. 33 (2011), pp. 2153-2160.
[50] W.E. Ranz, and W.R. Marshall, *Evaporation from drops*, Chem. Eng. Prog. 48 (1952), pp. 141-146.
[51] S. Chandrasekhar, *Radiative transfer*, Dover Publications, New York, 1960.
[52] K.D. Wan, Z.H. Wang, Y. He, J. Xia, Z.J. Zhou, J.H. Zhou, and K.F. Cen, *Experimental and modeling study of pyrolysis of coal, biomass and blended coal–biomass particles*, Fuel 139 (2015), pp. 356-364.
[53] T.F. Smith, Z.F. Shen, and J.N. Friedman, *Evaluation of Coefficients for the Weighted*

Sum of Gray Gases Model, J. Heat Transfer 104 (1982), pp. 602-608.
[54] D.M. Grant, R.J. Pugmire, T.H. Fletcher, and A.R. Kerstein, *Chemical-Model of Coal Devolatilization Using Percolation Lattice Statistics*, Energy Fuels 3 (1989), pp. 175-186.
[55] D. Genetti, T.H. Fletcher, and R.J. Pugmire, *Development and application of a correlation of 13C NMR chemical structural analyses of coal based on elemental composition and volatile matter content*, Energy Fuels 13 (1999), pp. 60-68.
[56] D.B. Genetti, *An advanced model of coal devolatilization based on chemical structure*. M.S. Thesis, Brigham Young University, 1999.
[57] Z.H. Wang, K.D. Wan, J. Xia, Y. He, Y.Z. Liu, and J.Z. Liu, *Pyrolysis Characteristics of Coal, Biomass, and Coal–Biomass Blends under High Heating Rate Conditions: Effects of Particle Diameter, Fuel Type, and Mixing Conditions*, Energy Fuels 29 (2015), pp. 5036-5046.
[58] M.M. Baum, and P.J. Street, *Predicting the combustion behaviour of coal particles*, Combust. Sci. Technol. 3 (1971), pp. 231-243.
[59] C.K. Westbrook, and F.L. Dryer, *Simplified Reaction Mechanisms for the Oxidation of Hydrocarbon Fuels in Flames*, Combust. Sci. Technol. 27 (1981), pp. 31-43.
[60] J. Milewski, K. Świrski, M. Santarelli, and P. Leone, *Advanced methods of solid oxide fuel cell modeling*, Springer-Verlag London, 2011.
[61] J. Galpin, A. Naudin, L. Vervisch, C. Angelberger, O. Colin, and P. Domingo, *Large-eddy simulation of a fuel-lean premixed turbulent swirl-burner*, Combust. Flame 155 (2008), pp. 247-266.
[62] X.D. Liu, S. Osher, and T. Chan, *Weighted essentially non-oscillatory schemes*, J. Comput. Phys. 115 (1994), pp. 200-212.
[63] V. Mittal, and H. Pitsch, *A flamelet model for premixed combustion under variable pressure conditions*, Proc. Combust. Inst. 34 (2013), pp. 2995-3003.
[64] M. Taniguchi, H. Okazaki, H. Kobayashi, S. Azuhata, H. Miyadera, H. Muto, and T. Tsumura, *Pyrolysis and ignition characteristics of pulverized coal particles*, J. Energy Resour. Technol. 123 (2001), pp. 32-38.
[65] C.D. Pierce, and P. Moin, *Method for generating equilibrium swirling inflow conditions*, AIAA J. 36 (1998), pp. 1325-1327.
[66] S. Badzioch, and P.G.W. Hawksley, *Kinetics of thermal decomposition of pulverized coal particles*, Ind. Eng. Chem. Proc. Des. Dev. 9 (1970), pp. 521-530.
[67] P.J. Van Eyk, P.J. Ashman, Z.T. Alwahabi, and G.J. Nathan, *The release of water-bound and organic sodium from Loy Yang coal during the combustion of single particles in a flat flame*, Combust. Flame 158 (2011), pp. 1181-1192.
[68] A. Saltelli, M. Ratto, T. Andres, F. Campolongo, J. Cariboni, D. Gatelli, M. Saisana, and S. Tarantola, *Global sensitivity analysis: the primer*, John Wiley & Sons, 2008.
[69] J.E.P. Navalho, J.M.C. Pereira, A.R. Ervilha, and J.C.F. Pereira, *Uncertainty quantification in the catalytic partial oxidation of methane*, Combust. Theory Model. 17 (2013), pp. 1067-1095.
[70] I.M. Sobol', and E.E. Myshetskaya, *Monte Carlo estimators for small sensitivity indices*, Monte Carlo Methods and Applications 13 (2008), pp. 455-465.

[71] I.M. Sobol', *Global sensitivity indices for nonlinear mathematical models and their Monte Carlo estimates*, Mathematics and Computers in Simulation 55 (2001), pp. 271-280.

Table 1. Coefficients of the progress variable for sodium reactions.

Species	α_i
Na	0.0
NaO	$M_{NA}/M_{NAO} = 23.0/39.0$
NaO_2	$M_{NA}/M_{NAO2} = 23.0/55.0$
NaOH	$M_{NA}/M_{NAOH} = 23.0/40.0$
$Na_2O_2H_2$	$2M_{NA}/M_{NA2O2H2} \times 10^4 = 46.0/80.0 \times 10^4$

Table 2. Operating conditions.

	Primary jet	Preheated gas
Average velocity (m/s)	10	4.8
Temperature (K)	300	1510
Mass fraction		
N_2	0.768	0.760
O_2	0.232	0.101
CO_2	0.0	0.093
H_2O	0.0	0.045

Table 3. Coal analysis [19].

Ultimate analysis (dry-ash-free basis, wt%)	
C	83.1
H	4.6
O	9.9
N	1.9
S	0.5
Proximate analysis (dry basis, wt%)	
Volatile matter	31.1
Fixed carbon	54.0
Ash	14.9

Table 4. Analysis of Loy Yang brown coal [67].

Dry basis, wt%	
C	67.8
H	5.20
N	0.57
S	0.24
Cl	0.06
Ash	0.80
O	25.3
In ash, wt%	
SiO_2	12.9
Al_2O_3	31.4
Fe_2O_3	6.70
TiO_2	0.70
K_2O	0.77
MgO	12.2
Na_2O	11.3
CaO	5.60
SO_3	16.9

Table 5. Uncertainty in input parameters of the sodium chemistry lookup table.

Uncertain	Mean values			Uncertainty range	
parameter	Fuel-lean	Stoichiometric	Fuel-rich	Limits	σ
ϕ	0.5	1.0	1.5	± 0.1	0.05
Y_{sodium} ($\times 10^{-5}$)	0.8	2.35	4.0	± 0.5	0.25
T (K)	1200	1850	1600	± 100	50
C	0.5	0.5	0.5	± 0.1	0.05

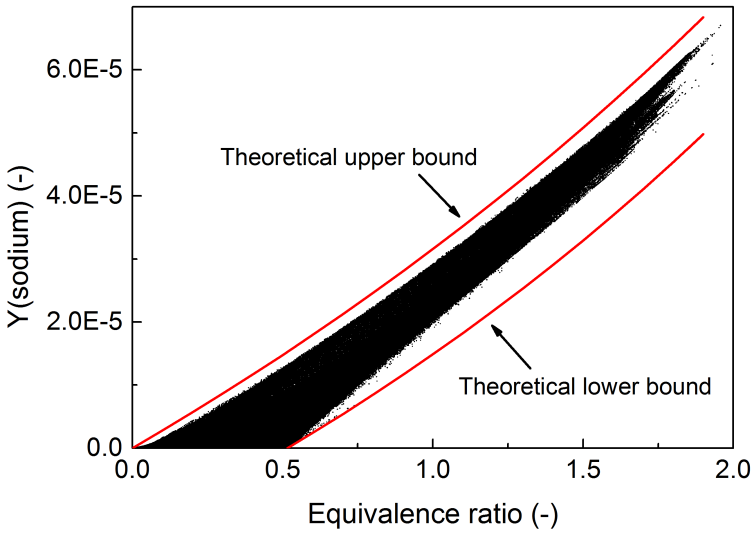

Figure 1. Sodium element mass fraction Y_{sodium} *vs* equivalence ratio ϕ. Scatter plot: LES results at one time instant. Lines: upper and lower bounds, which are used as the upper and lower limits of Y_{sodium} and ϕ in the chemical lookup table.

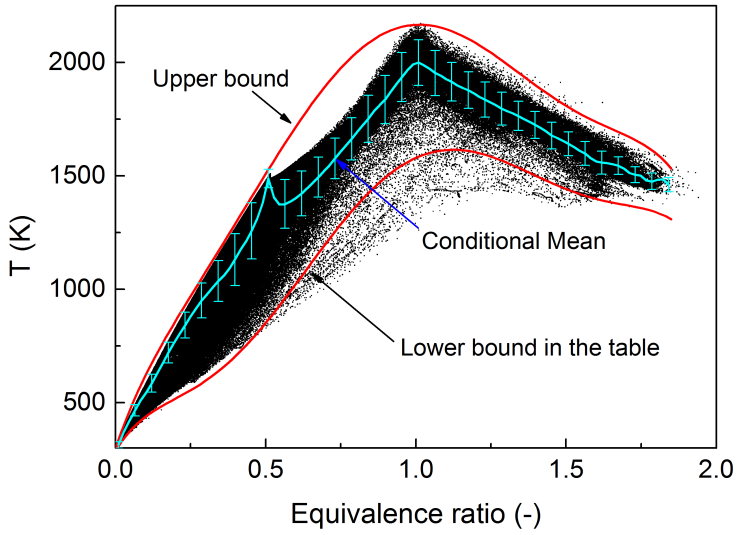

Figure 2. Gas-phase temperature *vs* equivalence ratio. Scatter plot: LES results at one time instant. Lines: upper and lower bounds used in the chemical lookup table, and the conditional mean and fluctuation of LES results.

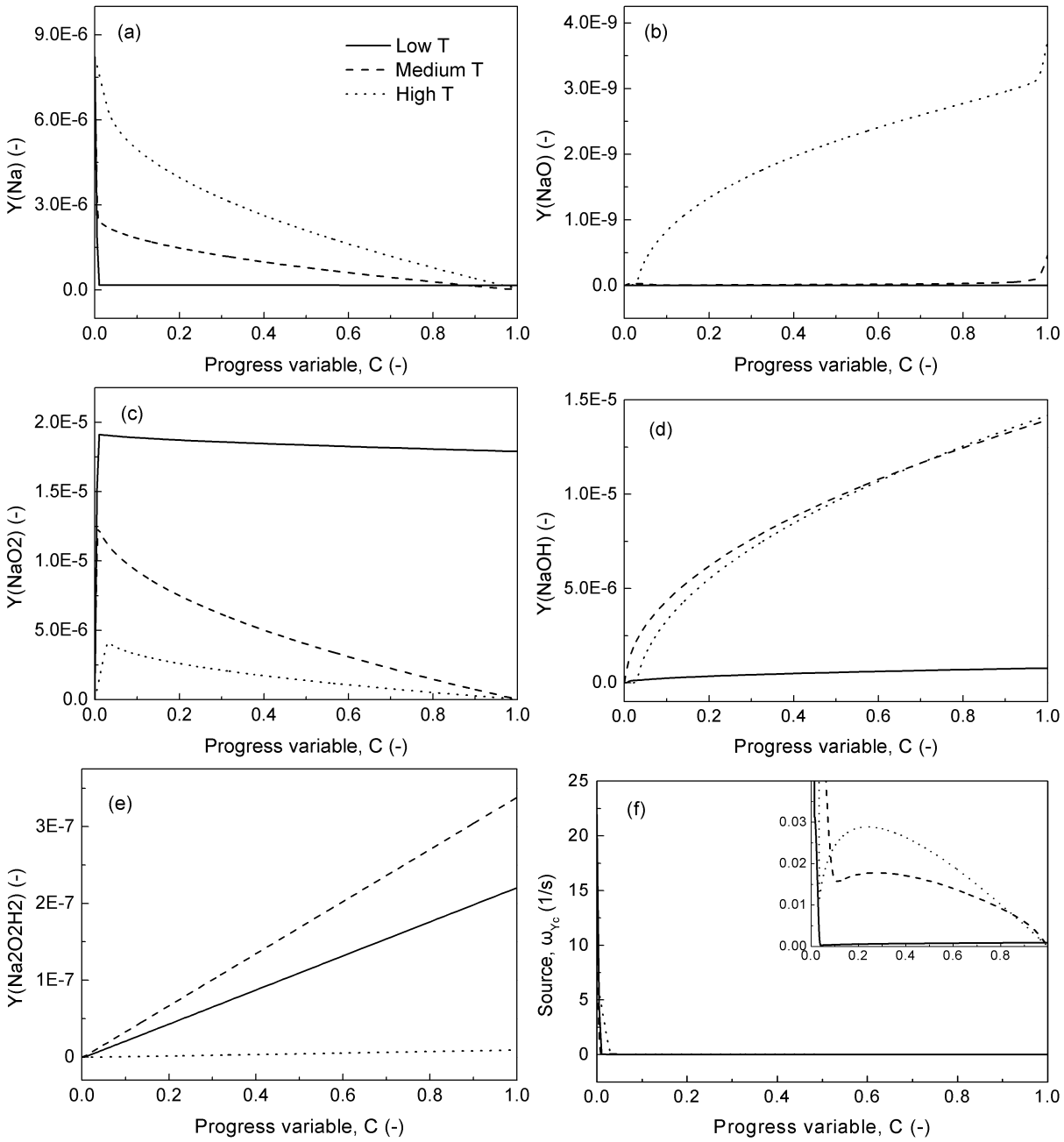

Figure 3. Species mass fractions and progress variable source *vs* progress variable at ϕ = 0.508 and Y_{sodium} = 0.82E-5. Solid line: T = 1005 K; Dashed line: 1208 K; Dotted line: 1396 K.

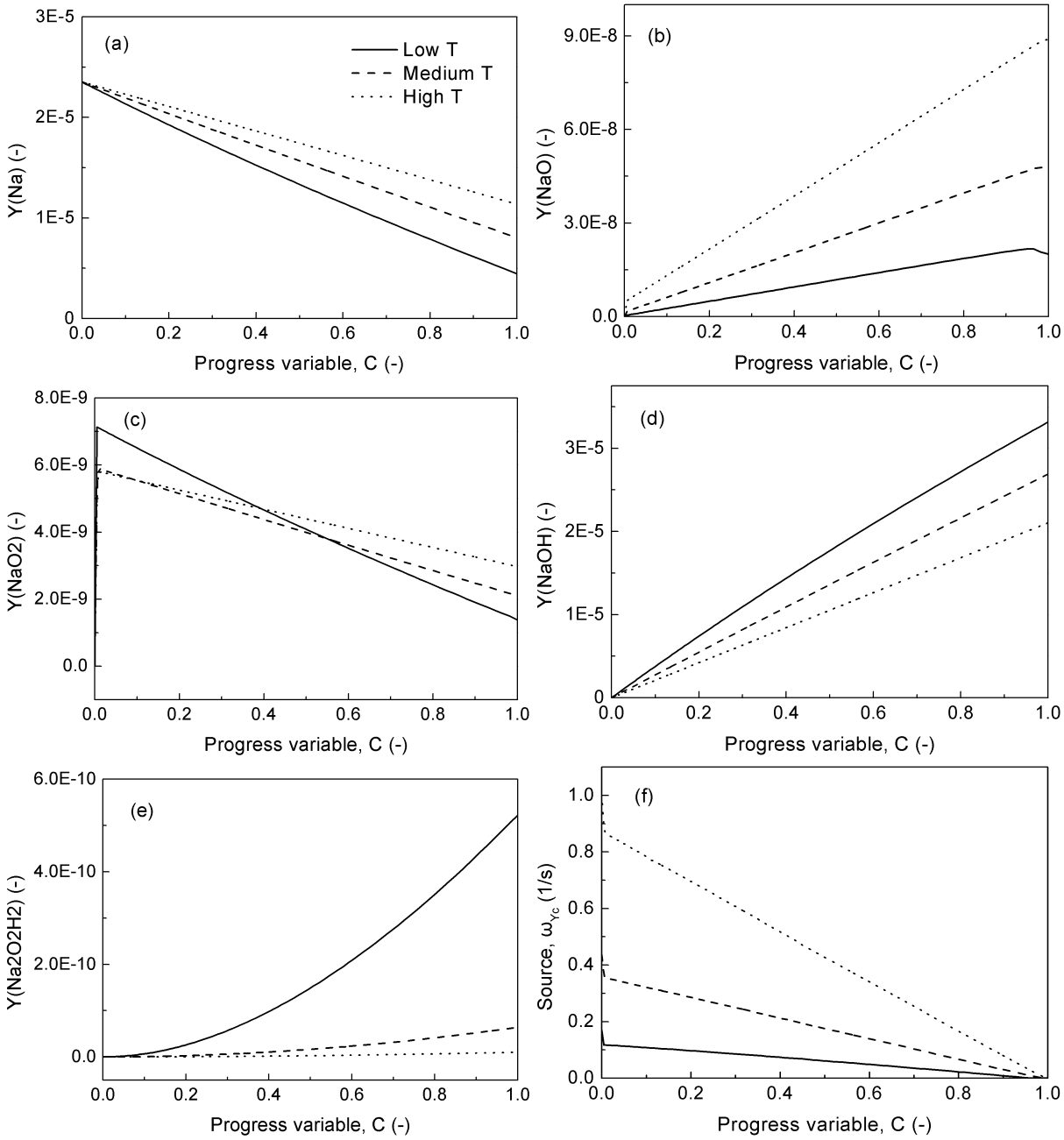

Figure 4. Species mass fractions and progress variable source *vs* progress variable at ϕ = 1.0 and Y_{sodium} = 2.35E-5. Solid line: T = 1721 K. Dashed line: 1878 K. Dotted line: 2022 K.

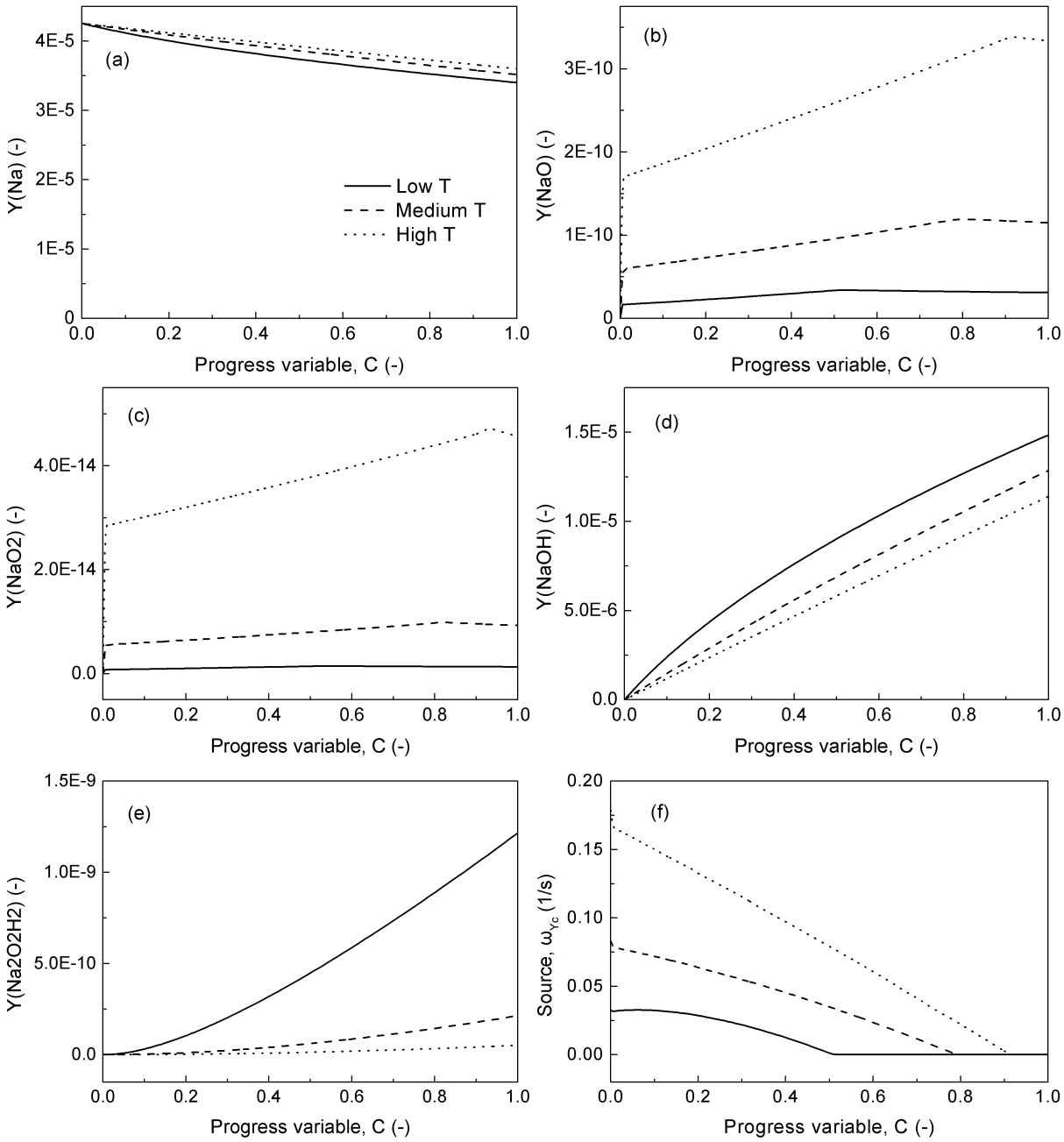

Figure 5. Species mass fractions and progress variable source *vs* progress variable at ϕ = 1.508 and Y_{sodium} = 4.26E-5. Solid line T = 1522 K. Dashed line: 1629 K. Dotted line: 1727 K.

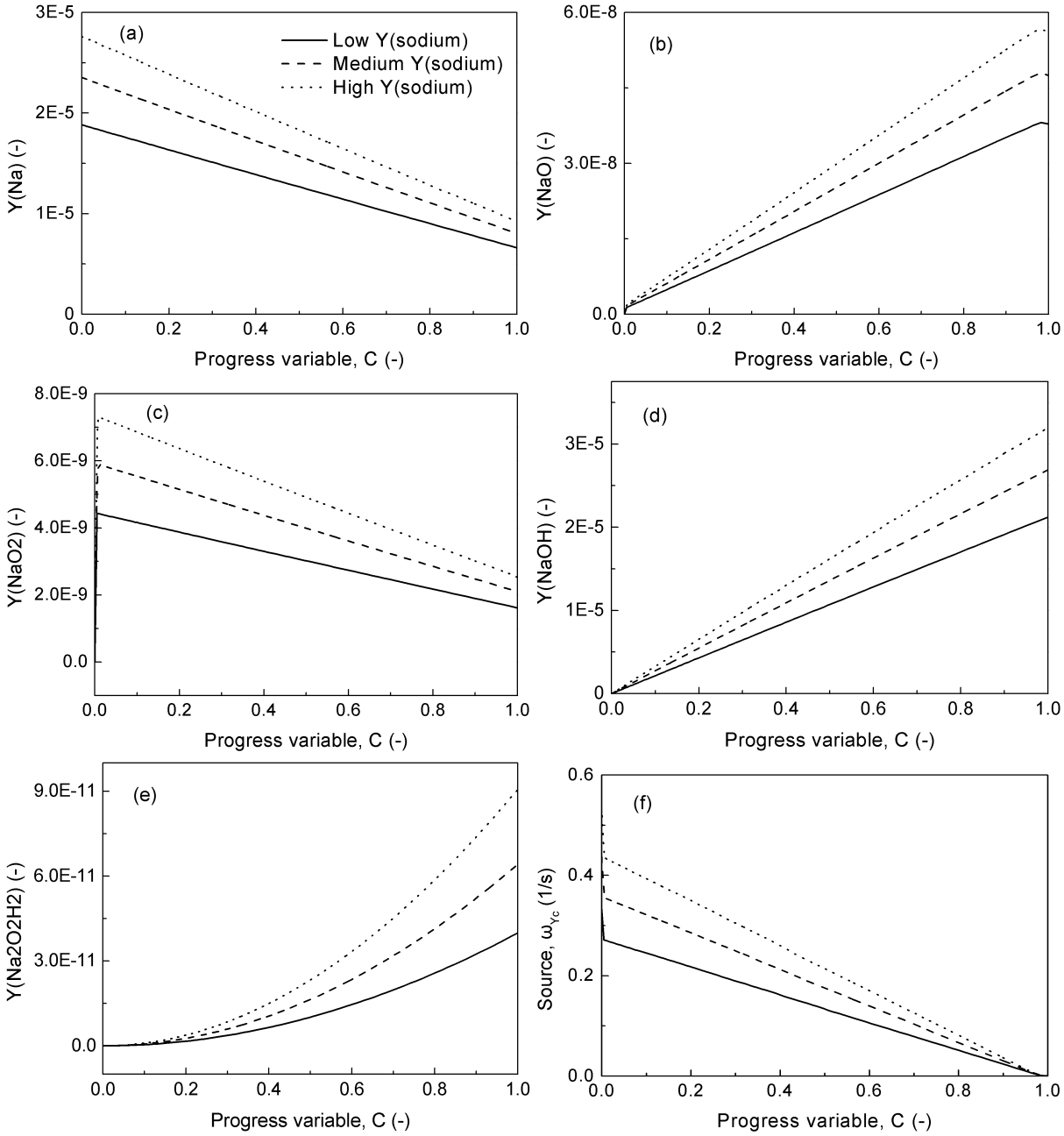

Figure 6. Species mass fractions and progress variable source *vs* progress variable at ϕ = 1.0 and T = 1878 K. Solid line: Y_{sodium} = 1.88E-5. Dashed line: 2.35E-5. Dotted line: 2.76E-5.

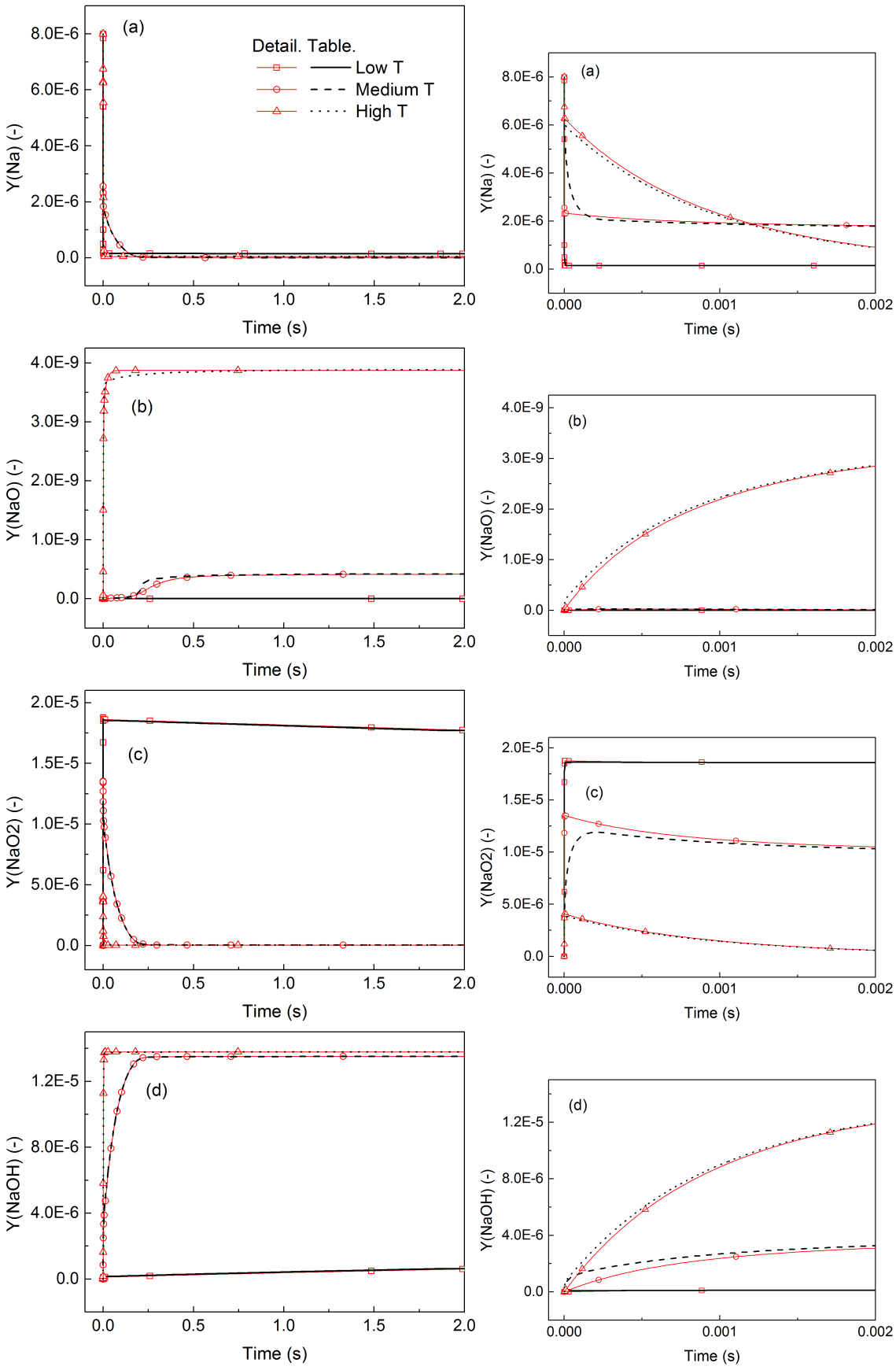
(a)
Detail. Table.
Low T
Medium T
High T
Y(Na) (-)
Time (s)
(b)
Y(NaO) (-)
(c)
Y(NaO2) (-)
(d)
Y(NaOH) (-)

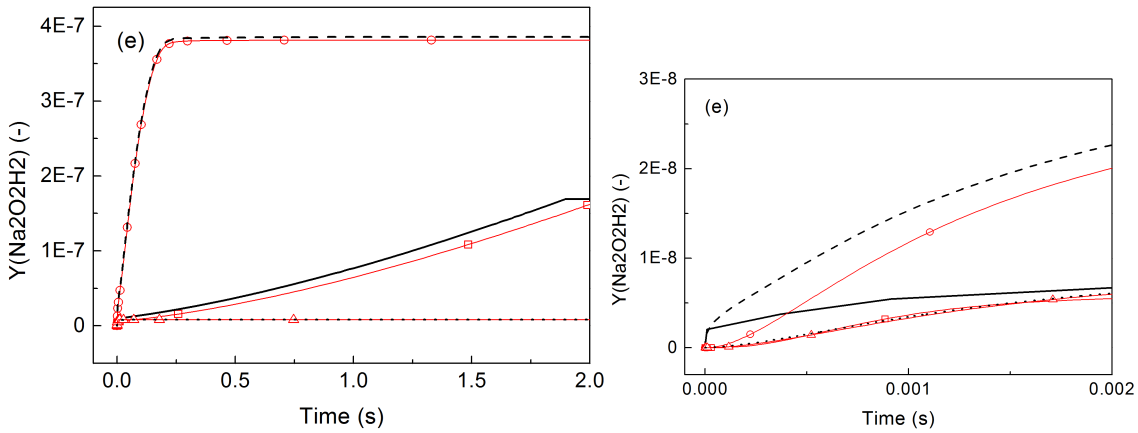

Figure 7. Species mass fractions versus time. Symbols: solving detailed mechanism [13]. Lines: solving progress variable. Square and solid-line: T = 1000 K; Circle and dashed-line: 1200 K; Triangle and dotted-line: 1400 K. ϕ = 0.493 and Y_{sodium} = 0.8E-5. The first-stage stiff evolutions are zoomed in and shown on the right side.

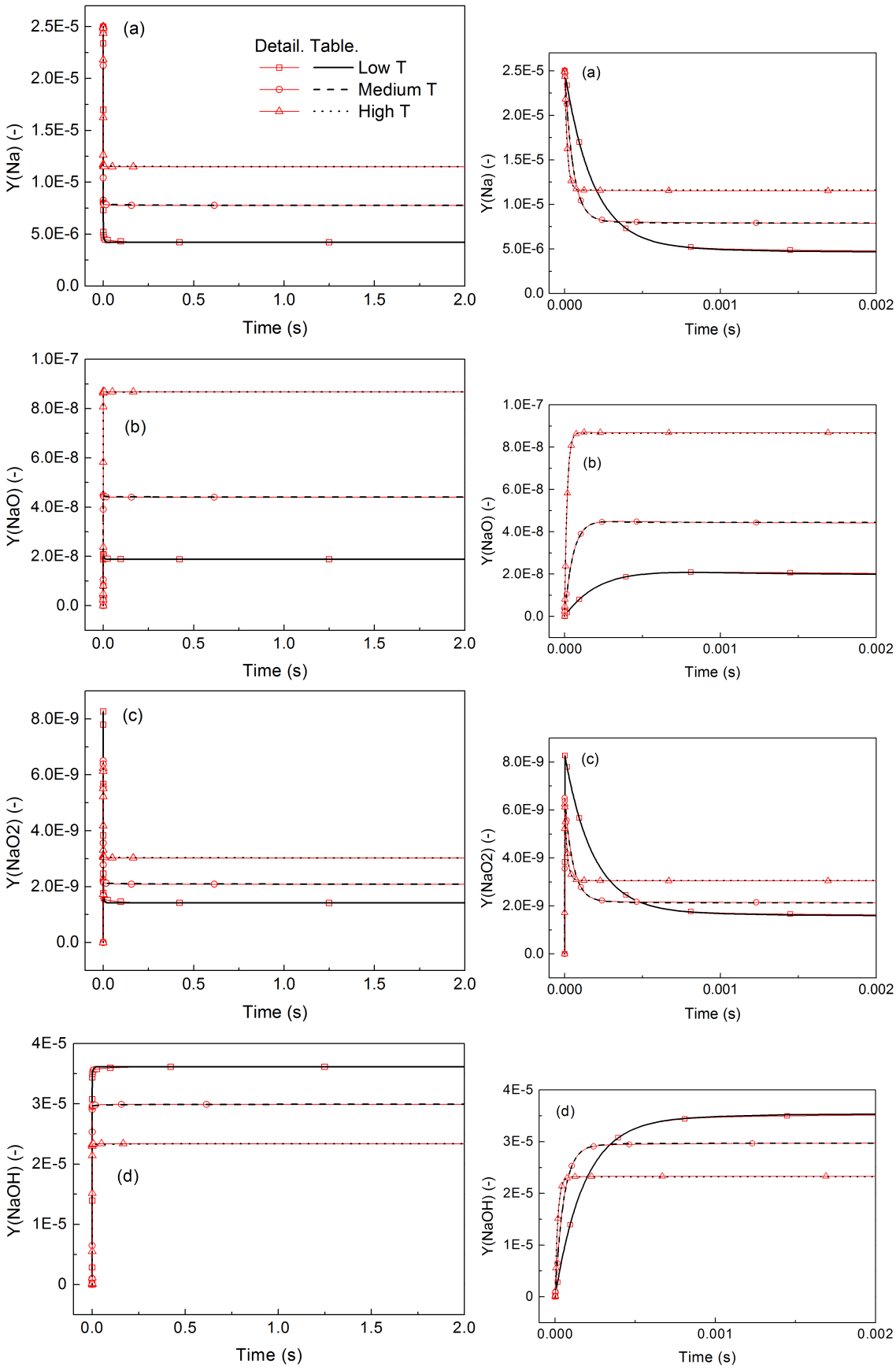
(a)
Detail. Table.
Low T
Medium T
High T
Y(Na) (-)
Time (s)
(b)
Y(NaO) (-)
(c)
Y(NaO2) (-)
(d)
Y(NaOH) (-)

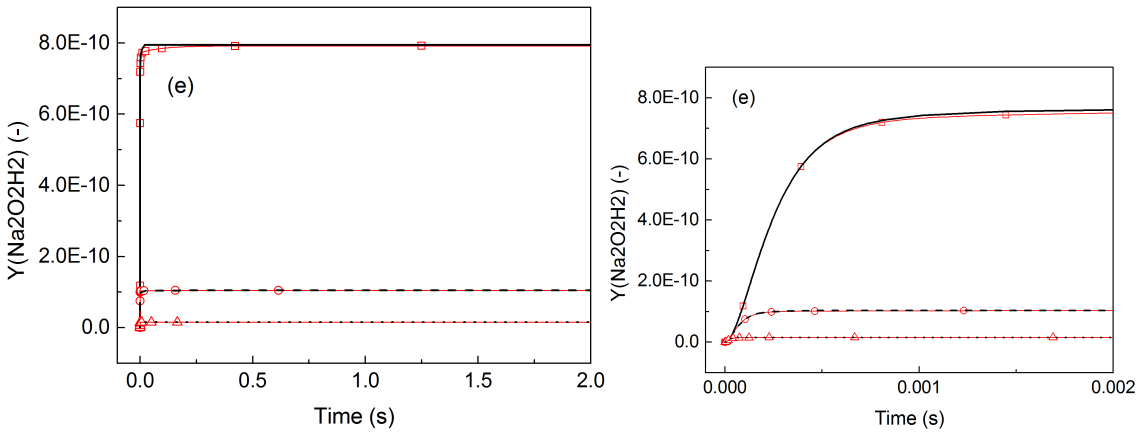

Figure 8. Species mass fractions versus time. Symbol: solving detailed mechanism [13]. Lines: solving progress variable. Square and solid-line: T = 1700 K; Circle and dashed-line: 1850 K; Triangle and dotted-line: 2000 K. ϕ = 1.0 and Y_{sodium} = 2.5E-5. The first-stage stiff evolutions are zoomed in and shown on the right side.

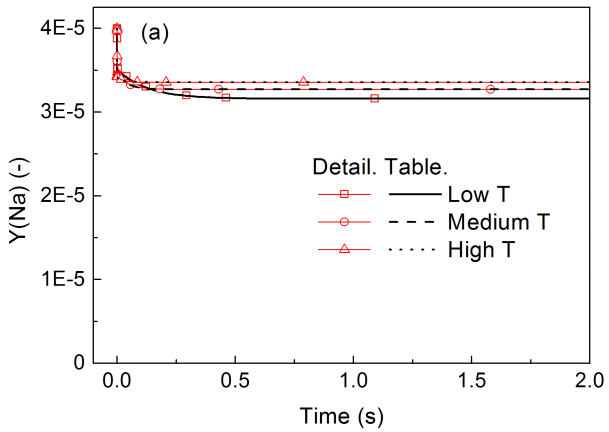
(a)
Detail. Table.
Low T
Medium T
High T
Y(Na) (-)
Time (s)

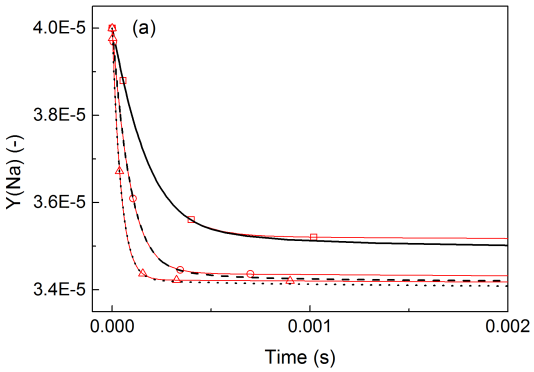
(a)
Y(Na) (-)
Time (s)

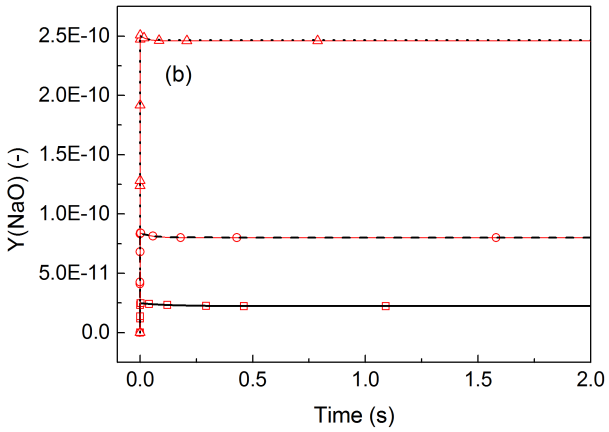
(b)
Y(NaO) (-)
Time (s)

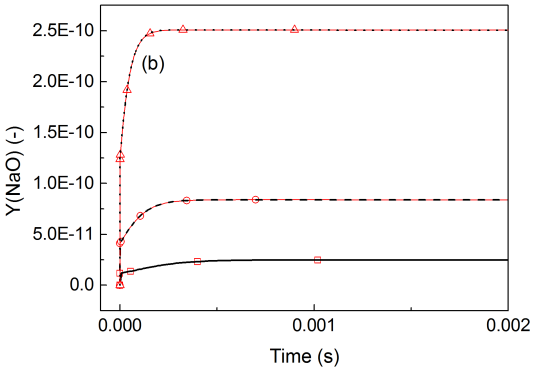
(b)
Y(NaO) (-)
Time (s)

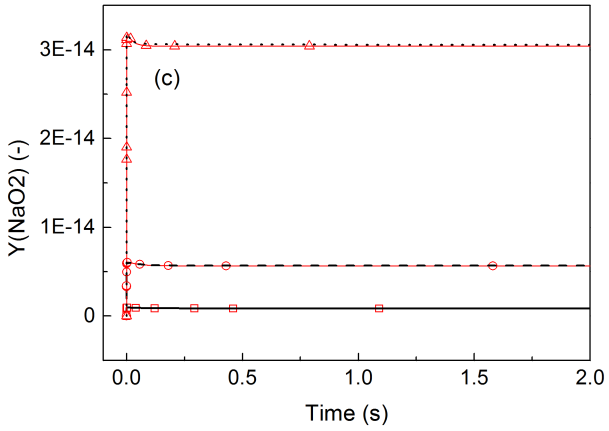
(c)
Y(NaO2) (-)
Time (s)

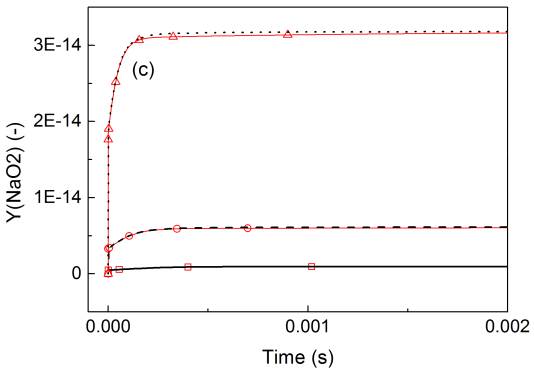
(c)
Y(NaO2) (-)
Time (s)

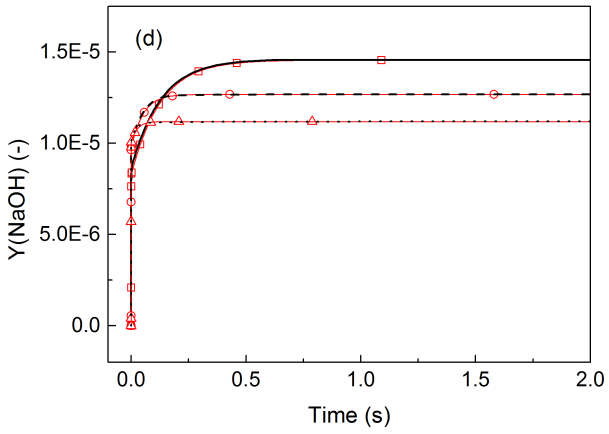
(d)
Y(NaOH) (-)
Time (s)

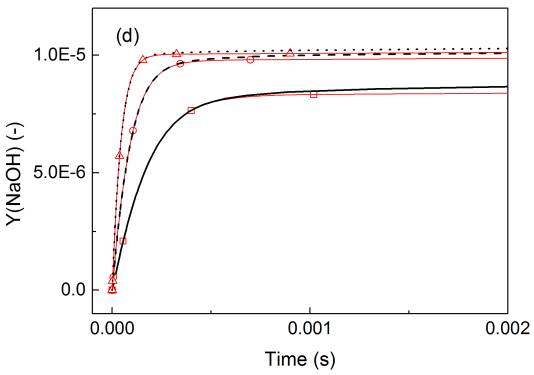
(d)
Y(NaOH) (-)
Time (s)

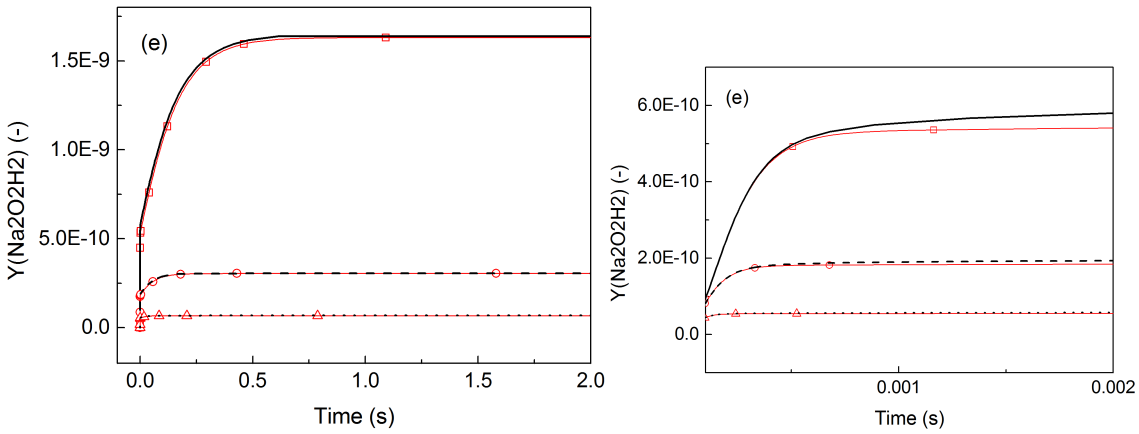

Figure 9. Species mass fractions versus time. Symbol: solving detailed mechanism [13]. Lines: solving progress variable. Square and solid-line: T = 1500 K; Circle and dashed-line: 1600 K; Triangle and dotted-line: 1700 K. ϕ = 1.494 and Y_{sodium} = 4.0E-5. The first-stage stiff evolutions are zoomed in and shown on the right side.

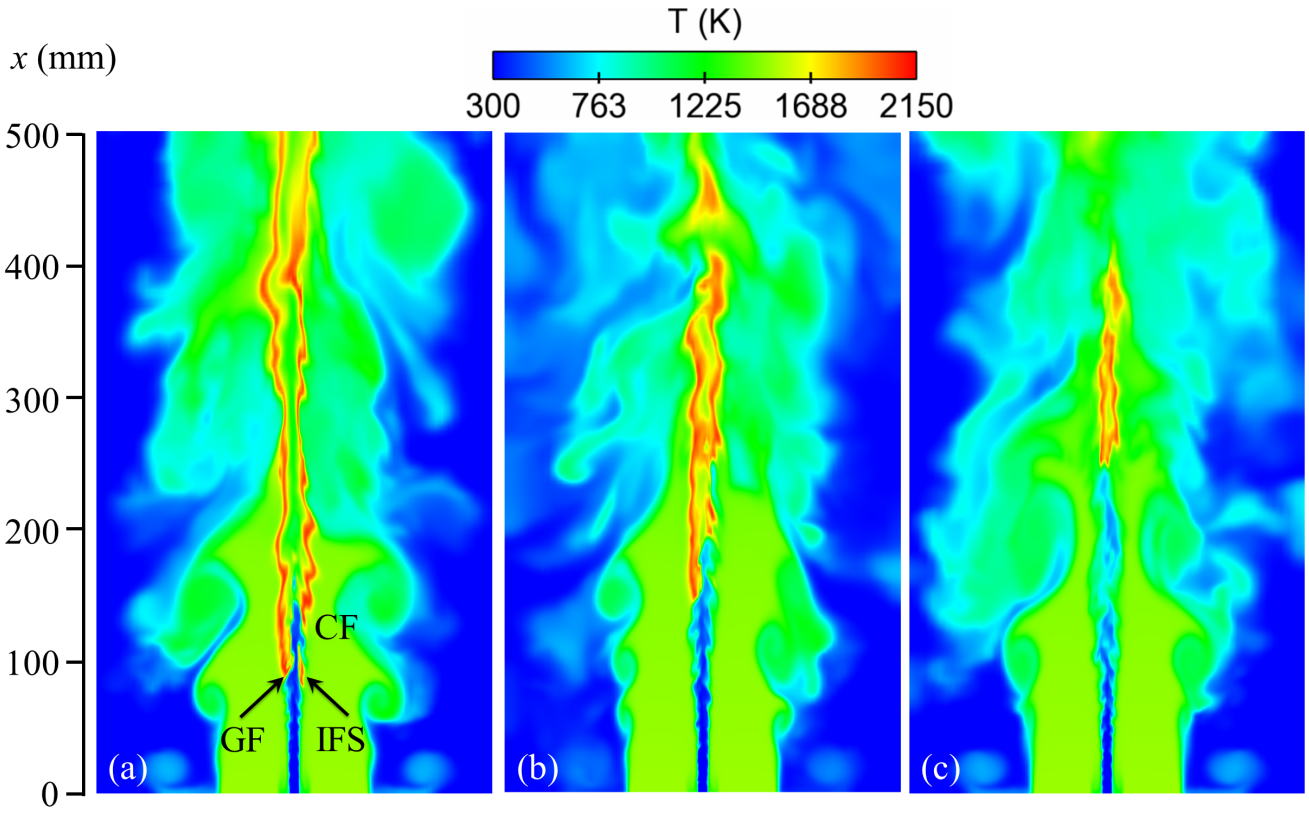

Figure 10. 2D snapshot of instantaneous gas temperature fields for SR = 0.14 (a), 0.22 (b) and 0.36. (c).

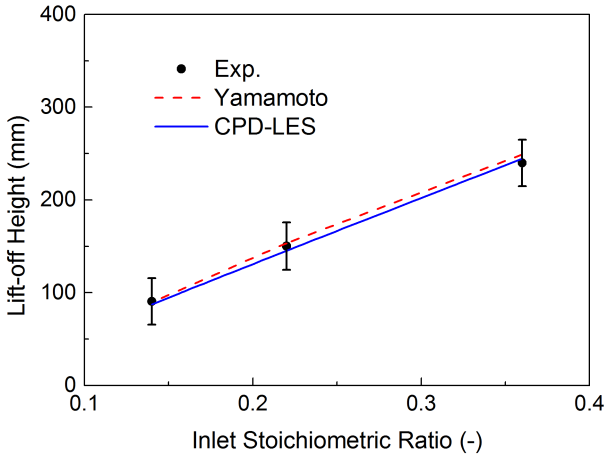

Figure 11. Comparison of the lift-off height at the three SRs.

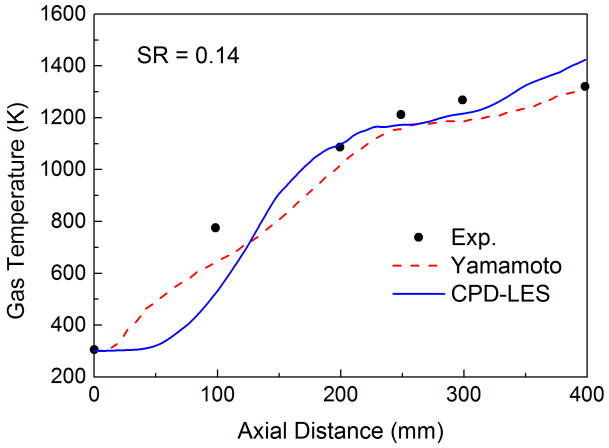

Figure 12. Averaged gas temperature along the jet centerline.

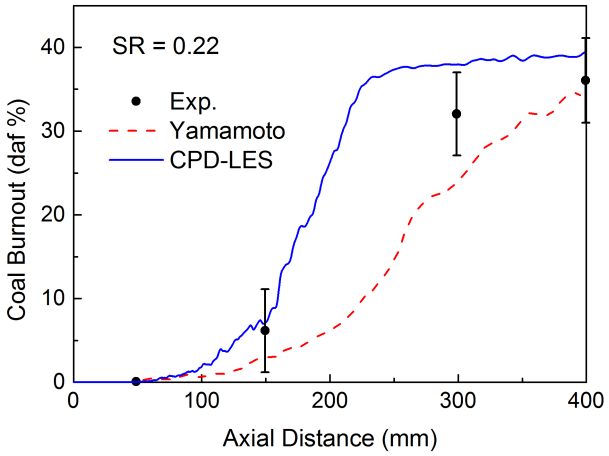

Figure 13. Coal burnout (%) along the jet centerline.

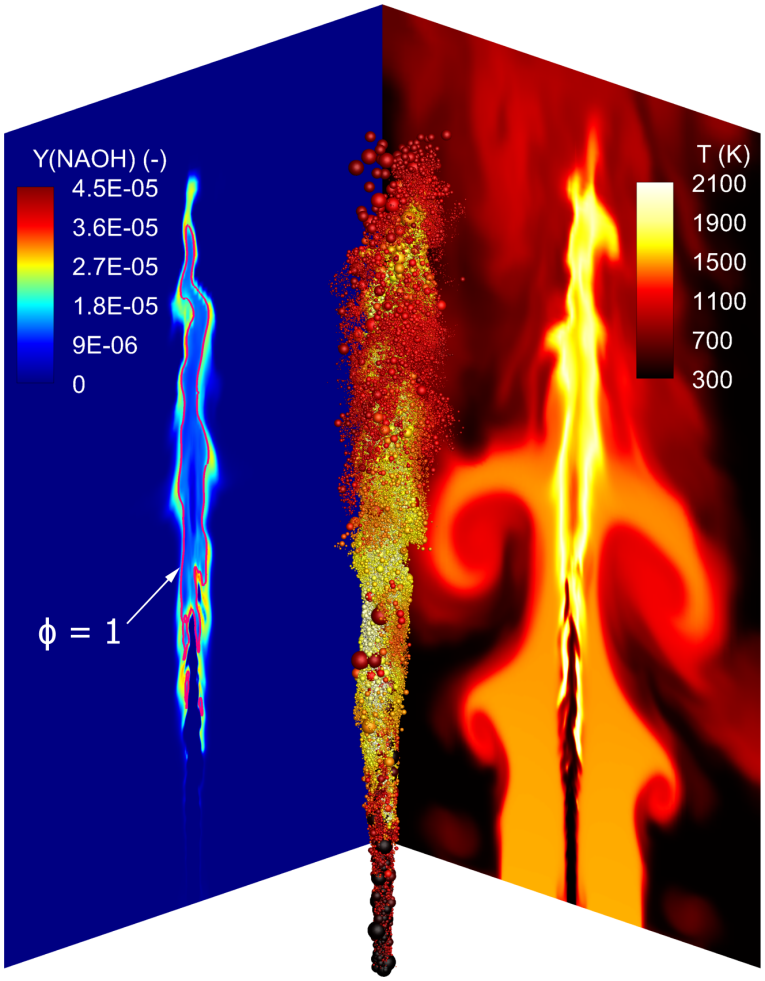

Figure 14. Instantaneous pulverized-coal particle distribution. Mass fraction of NaOH (left) and gas-phase temperature (right), 2D snapshot through the jet centerline. The pulverized-coal particles are colored by the particle temperature. The size of coal particles is also illustrated. The diameter of the largest particle is 180 μm.

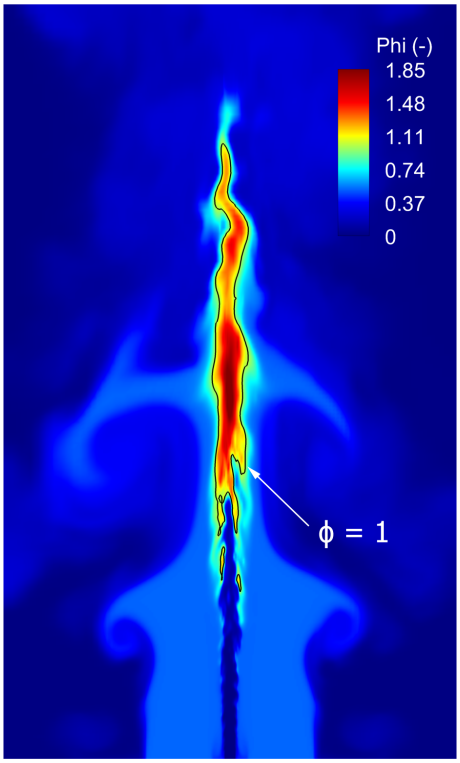

Figure 15. 2D snapshot of the equivalence ratio (ϕ).

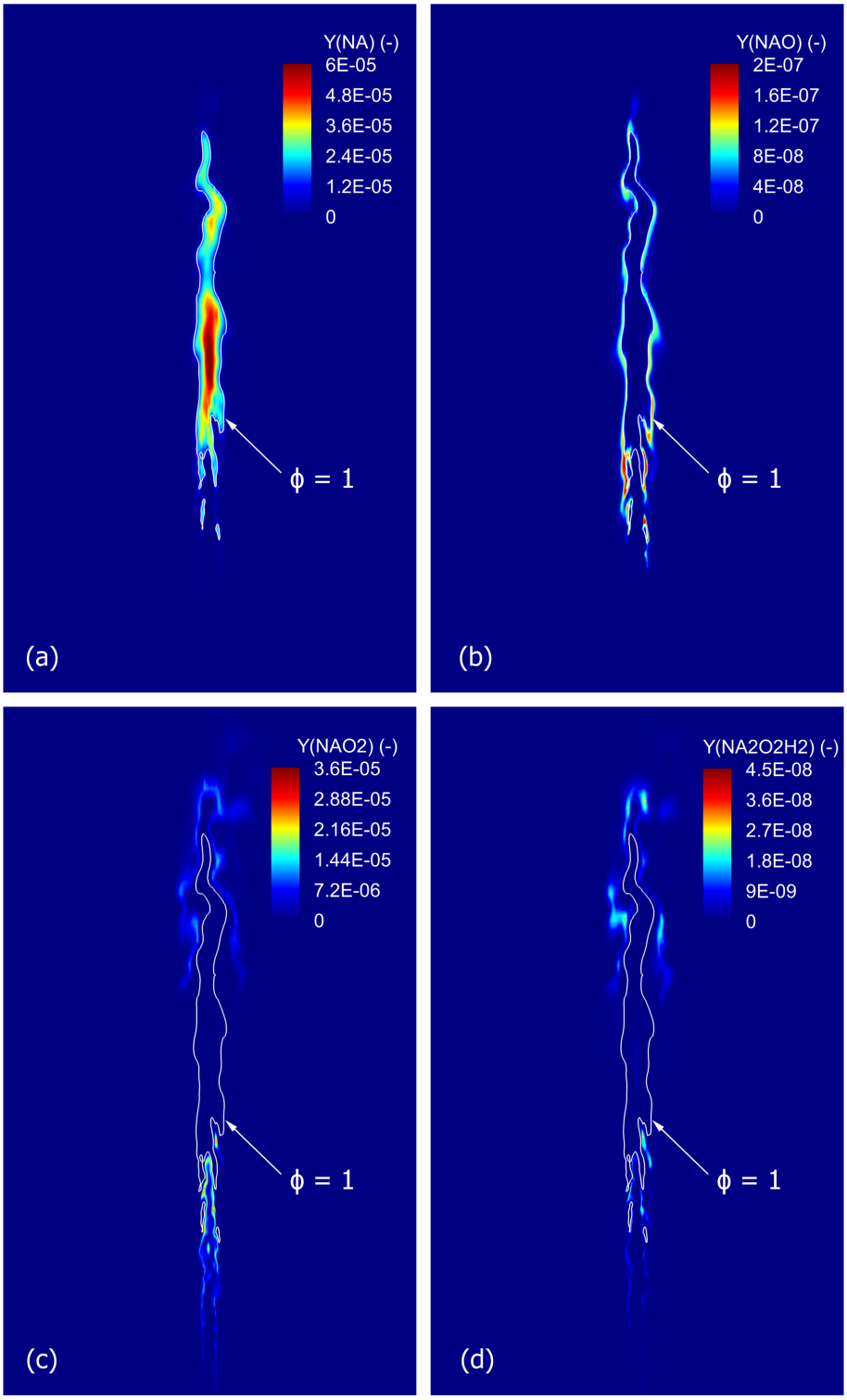

Figure 16. 2D snapshots of the mass fractions of (a) Na, (b) NaO, (c) NaO_2, and (d) $Na_2O_2H_2$.

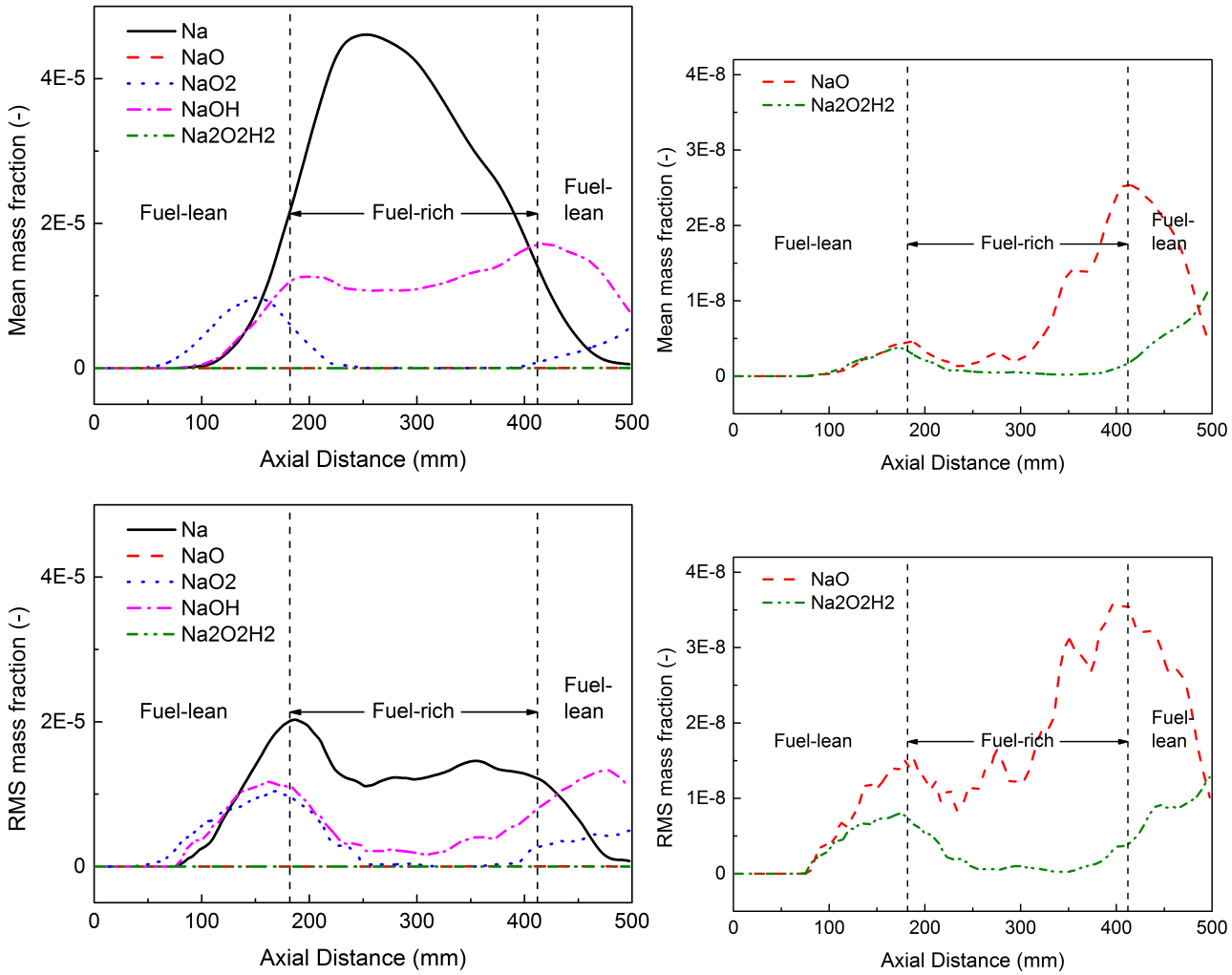

Figure 17. Mean and RMS mass fractions of the 5 sodium species along the jet centerline. The profiles for the two minor species NaO and $Na_2O_2H_2$ are zoomed in and shown on the right side.

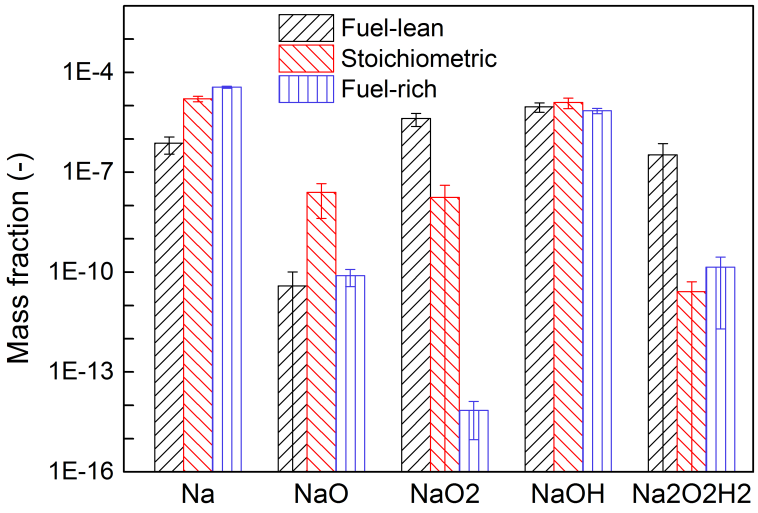

Figure 18. The response mass fractions of the 5 sodium species from the chemistry table under the fuel-lean, stoichiometric and fuel-rich conditions. In some cases, the lower end of the error bar is not shown because the standard deviation is larger than the mean value.

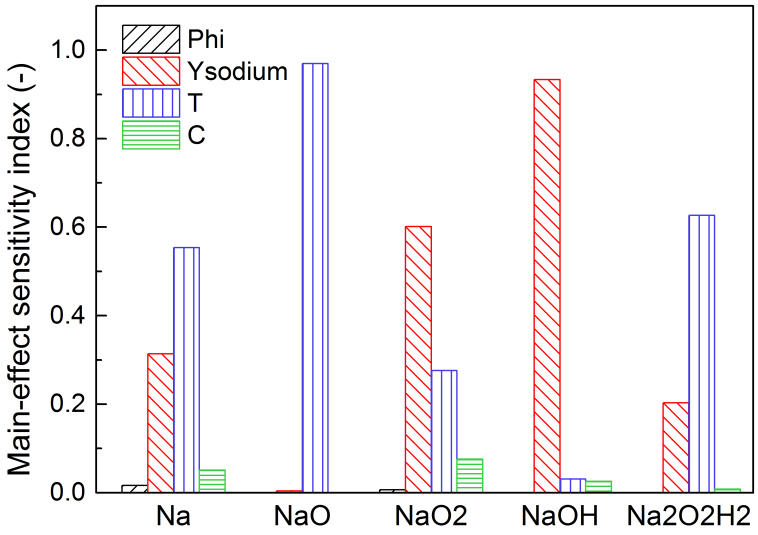

Figure 19. Main-effect sensitivity indices for the 5 sodium species under the fuel-lean condition.

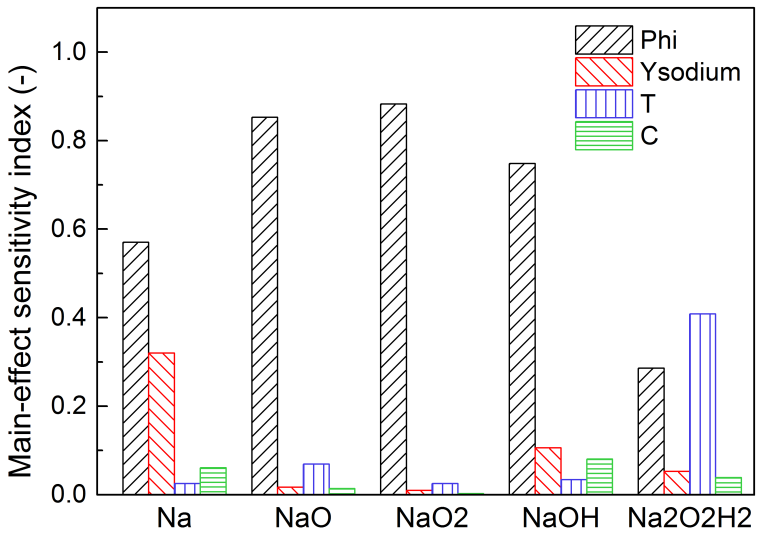

Figure 20. Main-effect sensitivity indices for the 5 sodium species under the stoichiometric condition.

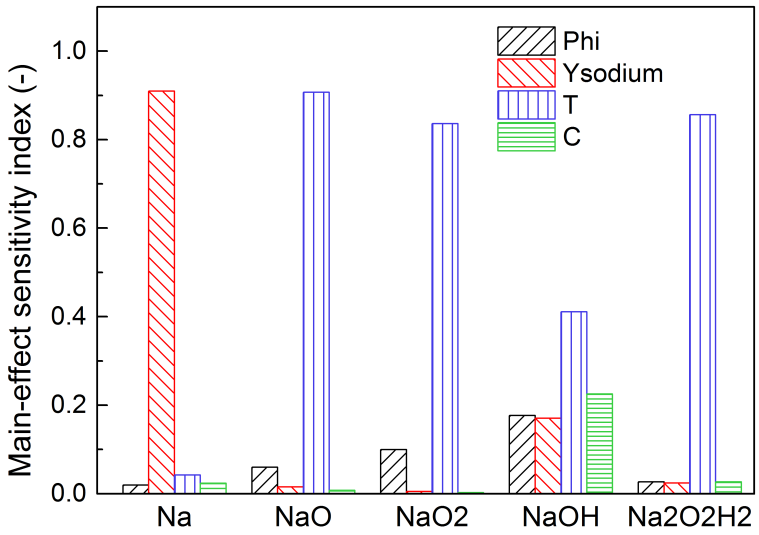

Figure 21. Main-effect sensitivity indices for the 5 sodium species under the fuel-rich condition.

Figure captions

Figure 1. Sodium element mass fraction Y_{sodium} *vs* equivalence ratio ϕ. Scatter plot: LES results at one time instant. Lines: upper and lower bounds, which are used as the upper and lower limits of Y_{sodium} and ϕ in the chemical lookup table.

Figure 2. Gas-phase temperature *vs* equivalence ratio. Scatter plot: LES results at one time instant. Lines: upper and lower bounds used in the chemical lookup table, and the conditional mean and fluctuation of LES results.

Figure 3. Species mass fractions and progress variable source *vs* progress variable at ϕ = 0.508 and Y_{sodium} = 0.82E-5. Solid line: T = 1005 K; Dashed line: 1208 K; Dotted line: 1396 K.

Figure 4. Species mass fractions and progress variable source *vs* progress variable at ϕ = 1.0 and Y_{sodium} = 2.35E-5. Solid line: T = 1721 K. Dashed line: 1878 K. Dotted line: 2022 K.

Figure 5. Species mass fractions and progress variable source *vs* progress variable at ϕ = 1.508 and Y_{sodium} = 4.26E-5. Solid line T = 1522 K. Dashed line: 1629 K. Dotted line: 1727 K.

Figure 6. Species mass fractions and progress variable source *vs* progress variable at ϕ = 1.0 and T = 1878 K. Solid line: Y_{sodium} = 1.88E-5. Dashed line: 2.35E-5. Dotted line: 2.76E-5.

Figure 7. Species mass fractions versus time. Symbols: solving detailed mechanism [13]. Lines: solving progress variable. Square and solid-line: T = 1000 K; Circle and dashed-line: 1200 K; Triangle and dotted-line: 1400 K. ϕ = 0.493 and Y_{sodium} = 0.8E-5. The first-stage stiff evolutions are zoomed in and shown on the right side.

Figure 8. Species mass fractions versus time. Symbol: solving detailed mechanism [13]. Lines: solving progress variable. Square and solid-line: T = 1700 K; Circle and dashed-line: 1850 K; Triangle and dotted-line: 2000 K. ϕ = 1.0 and Y_{sodium} = 2.5E-5. The first-stage stiff evolutions are zoomed in and shown on the right side.

Figure 9. Species mass fractions versus time. Symbol: solving detailed mechanism [13]. Lines: solving progress variable. Square and solid-line: T = 1500 K; Circle and dashed-line: 1600 K; Triangle and dotted-line: 1700 K. ϕ = 1.494 and Y_{sodium} = 4.0E-5. The first-stage stiff evolutions are zoomed in and shown on the right side.

Figure 10. 2D snapshot of instantaneous gas temperature fields for SR = 0.14 (a), 0.22 (b) and 0.36. (c).

Figure 11. Comparison of the lift-off height at the three SRs.

Figure 12. Averaged gas temperature along the jet centerline.

Figure 13. Coal burnout (%) along the jet centerline.

Figure 14. Instantaneous pulverized-coal particle distribution. Mass fraction of NaOH (left) and gas-phase temperature (right), 2D snapshot through the jet centerline. The pulverized-coal particles are colored by the particle temperature. The size of coal particles is also illustrated. The diameter of the largest particle is 180 μm.

Figure 15. 2D snapshot of the equivalence ratio (ϕ).

Figure 16. 2D snapshots of the mass fractions of (a) Na, (b) NaO, (c) NaO_2, and (d) $Na_2O_2H_2$.

Figure 17. Mean and RMS mass fractions of the 5 sodium species along the jet centerline. The profiles for the two minor species NaO and $Na_2O_2H_2$ are zoomed in and shown on the right side.

Figure 18. The response mass fractions of the 5 sodium species from the chemistry table under the fuel-lean, stoichiometric and fuel-rich conditions. In some cases, the lower end of the error bar is not shown because the standard deviation is larger than the mean value.

Figure 19. Main-effect sensitivity indices for the 5 sodium species under the fuel-lean condition.

Figure 20. Main-effect sensitivity indices for the 5 sodium species under the stoichiometric condition.

Figure 21. Main-effect sensitivity indices for the 5 sodium species under the fuel-rich condition.

Color figures can be used for the online PDF version and the gray style for hardcopy reproduction.